



UNIVERSITY OF LEEDS

This is a repository copy of *Digital Design of Batch Cooling Crystallization Processes: Computational Fluid Dynamics Methodology for Modeling Free-Surface Hydrodynamics in Agitated Crystallizers*.

White Rose Research Online URL for this paper:

<https://eprints.whiterose.ac.uk/164154/>

Version: Accepted Version

Article:

Corzo, DMC, Ma, CY orcid.org/0000-0002-4576-7411, Mahmud, T orcid.org/0000-0002-6502-907X et al. (1 more author) (2020) Digital Design of Batch Cooling Crystallization Processes: Computational Fluid Dynamics Methodology for Modeling Free-Surface Hydrodynamics in Agitated Crystallizers. *Organic Process Research & Development*, 24 (11). pp. 2565-2582. ISSN 1083-6160

<https://doi.org/10.1021/acs.oprd.0c00240>

© 2020 American Chemical Society. This is an author produced version of an article published in *Organic Process Research and Development*. Uploaded in accordance with the publisher's self-archiving policy.

Reuse

Items deposited in White Rose Research Online are protected by copyright, with all rights reserved unless indicated otherwise. They may be downloaded and/or printed for private study, or other acts as permitted by national copyright laws. The publisher or other rights holders may allow further reproduction and re-use of the full text version. This is indicated by the licence information on the White Rose Research Online record for the item.

Takedown

If you consider content in White Rose Research Online to be in breach of UK law, please notify us by emailing eprints@whiterose.ac.uk including the URL of the record and the reason for the withdrawal request.



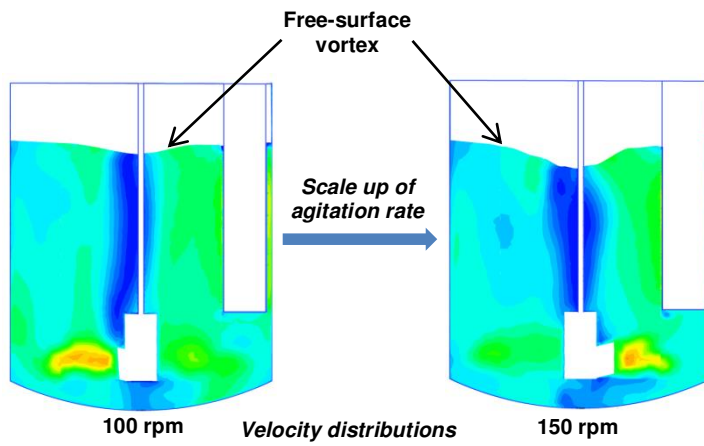
eprints@whiterose.ac.uk
<https://eprints.whiterose.ac.uk/>

Digital design of batch cooling crystallisation process: CFD methodology for modelling free-surface hydrodynamics in agitated crystallisers

Diana M. Camacho Corzo, Cai Y. Ma, Tariq Mahmud* and Kevin J. Roberts

*Centre for the Digital Design of Drug Products
School of Chemical and Process Engineering
University of Leeds
Leeds LS2 9JT, United Kingdom*

For Table of Contents Only



CFD prediction of hydrodynamics in a kilo-scale single baffled crystalliser as part of a workflow for the digital design of pharmaceutical crystallisation processes

ABSTRACT: A framework for the digital design of batch cooling crystallisation processes is presented comprising three stages which are based on different levels of process complexity, integrating crystalliser hydrodynamics with crystallisation kinetics and consequently with expected crystal size distribution. In the first stage of the framework, a CFD methodology is developed to accurately assess hydrodynamics in a typical batch crystalliser configuration, comprising a dish-bottom vessel with a single beavertail baffle agitated by a retreat curve impeller, used in the pharmaceutical as well as in the fine chemicals industries. The hydrodynamics of crystallisers with such configurations is characterised by vortex formation on the free liquid surface. It is therefore important to model the free surface using the Volume-of-Fluid (VoF) method. Comparison of the predicted mean velocity components with experimental measurements using Laser Doppler Anemometry reveals that improved predictions are obtained using a differential Reynolds-stress transport model for turbulence coupled with the VoF for modelling the gas-liquid interface compared with those using the Shear-stress transport model and with a flat liquid surface. This study demonstrates that an accurate treatment of the liquid free-surface for capturing vortex formation is essential for reliable predictions of the crystalliser's flow field. Whilst the vortex depth is predicted to increase with increasing impeller Reynolds number, the dependence of hydrodynamic macro-parameters, including power number, impeller flow number and secondary circulation flow number, on Reynolds number reveals that they are essentially constant within the turbulent regime, but fluctuate when the flow is in the transitional and laminar regime as fluid viscosity increases.

Keywords: Digital design workflow, Pharmaceutical crystalliser hydrodynamics, CFD of free-surface flow, volume-of-fluid method, turbulence modelling

1. INTRODUCTION

1.1 Background. Batch cooling crystallisation is a critical unit operation in the pharmaceutical as well as agrochemicals and fine chemicals industries used for the isolation and purification of active ingredients, thus the design of the crystalliser (i.e., vessel geometry/configuration and its internals), together with the selection of appropriate operating conditions, is vital for the production of crystals with required physical properties such as crystal size distribution (CSD), crystal shape, morphology, polymorphic form and purity. In the pharmaceutical industry, extensive experimental testing at a laboratory-, kilo- and pilot-scale is traditionally used for the development and scale-up of crystallisation processes in order to meet the critical quality attributes defined by the product specifications. The number of trials that can be carried out is severely restricted by the small quantity of materials usually available during the process development stage.^{1,2} Thus, applications of *quality-by-design* approaches using first-principles based modelling tools provide the opportunity for the development of validated workflow for the design, control and scale-up of crystallisation processes for the production of crystals meeting the highest quality standards regarding their resultant product form. The adoption of such in-silico tools, together with the concomitant reduction in the need for experimental work, could lead to faster regulatory approval, shorter product time to market and a significant reduction in R&D costs.

Pharmaceutical crystallisation processes are commonly performed in jacketed glass-lined vessels with either a conical or dish shaped (torispherical) bottom usually fitted with a single beavertail baffle away from the wall and the vessel content is agitated by a mixed-flow impeller such a retreat curved impeller (RCI).^{3,4} The hydrodynamic environment in agitated crystallisers is highly inhomogeneous, where the mean velocities and turbulence quantities may vary significantly particularly in large scale sizes (from the kilo through to an industrial scale). This can result in imperfect mixing and non-uniform distributions of process parameters such as solution

temperature, solute concentration and supersaturation which is the driving force for nucleation and crystal growth.

Traditionally, lumped-parameter mechanistic modelling approaches based on the solution of a population balance model (PBM) equation are used for predicting the CSD in batch agitated crystallisers (see for example, Costa et al.⁵, Kalbasenka et al.⁶ and Shaikh et al.⁷), which assume perfectly mixed conditions within the vessel leading to uniform distributions of process parameters at a given instance of time. This assumption is highly inadequate for modelling crystallisation particularly in large-scale crystallisers where the mixing intensity and related hydrodynamic (such as liquid/solid velocities, slurry density, solution density and viscosity) and process parameters can vary spatially in a significant manner throughout the vessel, resulting in an uneven distribution of supersaturation. This can lead, in turn, to the incorrect estimation of nucleation and crystal growth rates, hence the predicted crystal size and shape distributions. Related to this, the crystallisation kinetics are also inter-dependent on flow parameters such as turbulence kinetic energy, shear and energy dissipation rates as the supersaturation is determined by local micro-mixing, reaction and mass transfer rates.⁸ Therefore, precision design tools for crystallisation process development and scale-up demand a detailed knowledge of the distribution of these parameters. Accordingly, it is necessary to use a high-level distributed-parameter model based on multi-phase computational fluid dynamics (CFD) coupled with a PBM to capture the effect of non-uniform distributions of process parameters on the crystal properties. Such a first-principles based model can provide a robust design basis to optimise the process, in order to yield the crystalline particles with the desired attributes, through the integrated and coupled modelling of fluid dynamics and crystallisation process kinetics. Although this approach has been advocated a decade ago,^{1,2} it has not received adequate attention in the pharmaceutical crystallisation R&D. Mechanistic models based on the well-mixed assumption embedded in process modelling software, such as gPROMS platform, are still largely used in the industry.

1.2 Pharmaceutical Crystallisation Modelling Strategy. The overall workflow needed for the crystallisation process design is summarised in Figure 1, which highlights the modelling strategy comprising three stages with increasing complexity which will deliver information on the final product crystal properties such as particle size and/or shape distributions:

- CFD for crystalliser's hydrodynamics,
- Fully coupled CFD-1D PBM for the prediction of CSD,
- Morphological PBM^{9,10} solved within well-mixed zones established via CFD using a multi-zonal process modelling approach for the prediction of crystal size and shape distributions.

Stage 1: The first step involves the development of a reliable CFD methodology for the prediction of hydrodynamics in the crystalliser as well as the liquid-free surface profiles as a function of agitation rate and fluid properties enabling the determination of macro-parameters depended on fluid dynamics, such as power number (N_p), impeller flow number (N_d) and secondary circulation flow number (N_c).

Stage 2: The next step focuses on fully coupling a multi-phase CFD with 1D-PBM to predict CSD and to obtain an insight into the distributions of critical process parameters, such as supersaturation and slurry density, within the crystalliser. These will allow defining “well-mixed zones” and fluxes across the zone boundaries for a multi-zonal crystallisation process model. The well-mixed zones are defined as the regions of the crystalliser where relevant process parameters can be approximated as uniformly distributed.

Stage 3: Within the defined zones a morphological PBM^{9,10}, which is a multi-dimensional PBM for the predictions of crystal size and shape distributions, can be solved to obtain crystal size and shape distributions. This approach can be applied to different crystalliser scale sizes in order to derive scale-up equations in terms of appropriate parameters, such as impeller Reynolds number (Re), impeller tip velocity or power input per unit volume.

As depicted in Figure 1, a library of CFD data will be created which will contain distribution of well-mixed zone as a function of agitation rate, cooling rate, fluid physical properties and crystalliser scale sizes together with interzonal solid/liquid mass and heat flux, mass transfer rate and hydrodynamic macro-parameter data. This database can be readily uploaded onto a multi-zonal crystallisation process model, for example in the gCRYSTAL software environment, to facilitate the design and scale up of crystallisation processes.

As part of a large collaborative research project¹¹ with pharmaceutical industries and software developers, we are addressing the need for digitization of this industrial sector via developing first-principle based advanced modelling tools for the digital design of pharmaceutical crystallisation processes. This paper reports our initial (Stage 1) work aiming towards achieving this goal and focuses on the development and assessment of a state-of-the-art CFD methodology for reliable predictions of pharmaceutical batch crystalliser hydrodynamics. This approach can be extended to provide a strong basis for the development of digital design methodologies for continuous crystallisation processes which have captured a significant attention in the pharmaceutical industry in recent years.

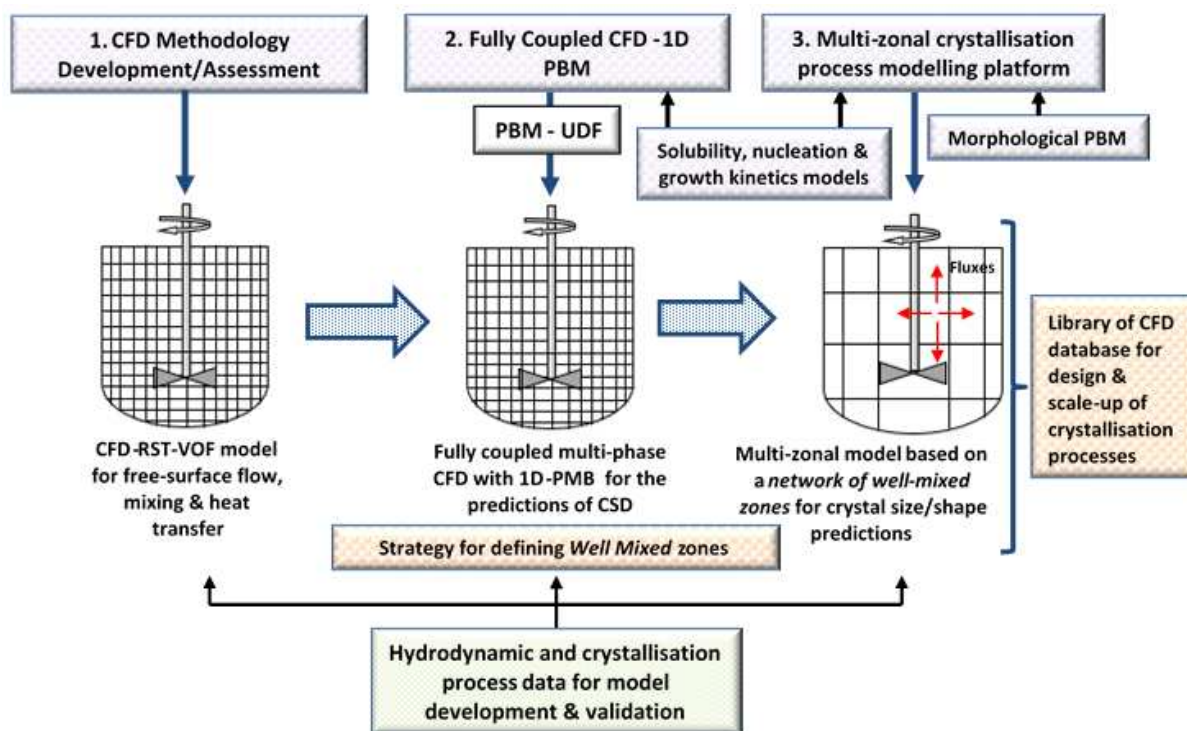


Figure 1. A workflow for the digital design of batch cooling crystallisation processes.

1.3 Previous Studies and Present Contributions. One of the primary features of unbaffled and partially baffled agitated vessels is the highly swirling liquid motion, which leads to the formation of a central vortex causing a depression in the liquid free-surface. For an improved accuracy of CFD predictions, it is important to model the shape of the liquid free-surface because it affects the flow field,^{12,13} as well as the area of heat transfer to the ullage region and at the vessel wall.¹⁴ Despite a widespread use of vessels with a single baffle agitated by a RCI in the pharmaceutical as well as in the fine chemicals industry, a limited body of work on their hydrodynamic and mixing performance has been reported; even basic information such as vortex depth, power and flow number correlations are rarely found in the open literature.

Previous studies have assessed the effect of agitation rates on the vortex profiles in unbaffled vessels. These studies, including that of Nagata,¹⁵ focused on the development of analytical equations for the prediction of vortex profiles by subdividing the vessel into two zones: the forced-vortex (or solid-body rotation) zone around the impeller shaft characterised by a linear

increase of the tangential velocity with the radial distance and an outer free-vortex zone characterised by a constant angular momentum. Smit and During¹⁶ modified Nagata's equations by introducing experimentally derived expressions for the tangential velocities in the forced- and free-vortex region to match the measured free-surface profiles. Busciglio et al.¹⁷ have found that the vortex shape strongly depends on the impeller type and suggested a simple model involving two parameters, a dimensionless distance and a correction to tangential velocity in the forced vortex region, dependent on the vessel geometry only. The predicted vortex shape using this model was in good agreement with their experimental data. In a recent study, Deshpande et al.¹⁸ have confirmed that whilst the vortex depth can be well described by Nagata's equation for a large Re (> 10,000), this model does not apply to smaller Re values which is the case for more viscous liquids, hence provided a new correlation which incorporates liquid viscosity, impeller size and speed and submergence. Limited studies have been concerned with the experimental determination of hydrodynamic macro-parameters (N_p , N_d and N_c) and their dependence on the agitation rate and crystalliser/reactor scale sizes in partially baffled vessels with a RCI. These include measurements of N_p in a laboratory-scale vessel with two beavertail baffles and computations of N_p , N_d and N_c using CFD in an industrial scale,^{19,20} measurements of N_p in laboratory-scale vessels with a single beavertail baffle^{21,22} and computations of N_p , N_d and N_c using CFD,²³ and measurements and CFD computations of N_p , as well as mixing time and solid suspension, in a laboratory-scale conical-based vessel with different baffling arrangements including a single beavertail baffle.²⁴ However, these studies lack a rigorous experimental validation of CFD predictions as these were compared only against the measured N_p .

A number of previous CFD studies have focused on the modelling of turbulent free-surface flow using the Volume-of-Fluid (VoF) method in unbaffled vessels agitated by radial-flow impellers (for example, Haque et al.¹³, Cartland Glover and Fitzpatrick²⁵, Haque et al.²⁶, Yang et al.²⁷ and Yang and Zhou²⁸) and in vessels with two beavertail baffles agitated by a RCI entering

from the bottom,^{29,30} and compared the predictions with the measurements of components of mean velocity and turbulence kinetic energy. In these studies using the RANS (Reynolds-averaged Navier-Stokes) approach, turbulence was represented using the standard k - ϵ ,^{13,25,26,28–30} Shear-stress transport (SST)^{13,26} and Reynolds-stress transport (RST)^{6,26,30} models. In more recent studies, detached-eddy simulation (DES)^{27,28} and large-eddy simulation (LES)²⁸ approaches have also been used. The free-surface profiles and the mean velocity components are generally well predicted by both the RANS and DES/LES approaches; however, the turbulence kinetic energy in the impeller stream is underpredicted by the former method. Li et al.³¹ carried out detailed velocity measurements using Laser Doppler Anemometry (LDA) in a 20 L dish-bottom vessel with a single beavertail baffle agitated by a RCI, representative of pharmaceutical crystallisers, at different speeds. They also performed CFD simulations of these experiments using the SST turbulence model assuming a flat liquid surface, which implies that a single baffle can suppress vortex formation. Even in the fully baffled vessels the liquid free surfaces are wavy with considerable deformation which needs to be modelled.^{12,32} This approach of Li et al.³¹ resulted in the underpredictions of the mean tangential velocity and turbulence kinetic energy. The hydrodynamic macro-parameters were also calculated²³ as a function of agitation rate revealing that the values of these parameters did not change significantly with increasing Re and became almost constant for $Re > 15,000$.

Building on our previous work on unbaffled agitated vessels,^{13,26} this study evaluates a RANS based CFD methodology for predicting the flow field and hydrodynamic macro-parameters for a typical pharmaceutical crystallisation system. For this purpose, we have selected the crystalliser which was previously used in our research group for hydrodynamic³¹ and batch cooling crystallisation³³ studies. Accordingly, within the strategy overviewed in Figure 1 this work represents the Stage 1 of the overall development and aims to provide a strong basis to link the hydrodynamics with the crystallisation process kinetics through the incorporation of these

parameters into first-principles models describing nucleation and crystal growth processes. A homogeneous multiphase flow model coupled with the VoF method is used to determine the liquid free-surface profiles and the flow fields at different agitator speeds. Calculations are performed with the eddy-viscosity based SST turbulence model and a second-moment RST model using the general purpose ANSYS Fluent-V17.1 CFD code. The computed mean velocity components and the turbulence kinetic energy are compared with LDA measurements of Li et al.³¹. Calculations hydrodynamic macro-parameters are also carried out as a function of the agitation rate and they are compared with data available in the literature.

2. CFD MODELLING METHODOLOGY

2.1 Governing Equations and Prediction Procedure for Free-surface flow.

The approach used in this study for the CFD simulation of flow in a single baffled agitated vessel with a free liquid surface in contact with a gas (in this case water and air) requires capturing the air-water interface and the calculation of the flow fields in both phases. To model this interaction, the VoF method is coupled with the Eulerian-Eulerian homogeneous multiphase flow model to determine the shape of the liquid surface and the flow fields, respectively. In this method both fluids share common velocity and turbulence fields within the whole computation domain, which is determined by solving a single set of governing transport equations with the volume weighted mixture density and viscosity. It is assumed that there is no entrainment of one fluid into the other. Thus, in the computational cells away from the air-water interface, the flow variables and fluid properties are representative of either air or water, and in the cells encompassing the interface they are representative of mixtures of the two phases depending on their volume fractions. This modelling approach was first used and validated in our previous study¹³ for the simulations of flow in unbaffled flat-bottom vessels agitated by a Rushton turbine and an eight-flat-bladed paddle

impeller and subsequently for a dish-bottom vessel with a Rushton turbine²⁶ and by other researchers in the field (e.g., Cartland Glover and Fitzpatrick²⁵ and Torr , et al.^{29,30}).

The turbulent flow calculations in agitated vessels are generally carried out through the numerical solution of three-dimensional, steady-state or time-dependent Reynolds-averaged Navier-Stokes and continuity equations. Turbulence model equations are solved to determine the Reynolds stress terms (i.e., turbulent momentum fluxes) in the RANS equations. An alternative approach which is expected to provide an improvement in the predictive accuracy, particularly for the turbulence quantities, but at the expense of a high computational cost is the LES method.³⁴ In this method, large eddies are resolved directly, whilst small eddies are modelled on the premise that these eddies are less dependent on the geometry and tend to be more isotropic. Previous modelling studies of flow in agitated vessels with and without baffles (for example, Yang et al.²⁷, Lamarque et al.³⁵, Hartmann et al.³⁶, Murthy and Joshi³⁷, Gimbun et al.³⁸, Joshi et al.³⁹ and Malika et al.⁴⁰) have demonstrated that the quality of mean flow field predictions, which affects the estimation of hydrodynamic macro-parameters, achieved through the LES method are generally comparable with those obtained with the RANS approach particularly with an anisotropic second-moment turbulence closure. However, the turbulence kinetic energy in the impeller stream is somewhat better predicted using this approach but not closely mimicking the measured trends. It is important to note that the application of LES for the modelling of industrial crystallisation processes can be computationally prohibitively expensive, therefore a pragmatic choice of turbulence modelling approach is necessary to expedite computation whilst accounting for the effect of turbulence with a reasonably good precision.

The time-dependent Reynolds-averaged continuity and Navier-Stokes equations in an inertial reference frame are described in concise form using the Cartesian tensor notation by:

$$\frac{\partial \rho_m}{\partial t} + \frac{\partial}{\partial x_i} (\rho_m u_i) = 0 \quad (1)$$

$$\frac{\partial}{\partial t}(\rho_m u_i) + \frac{\partial}{\partial x_j}(\rho_m u_i u_j) = -\frac{\partial P}{\partial x_i} + \frac{\partial}{\partial x_j} \left(\mu_m \left[\frac{\partial u_i}{\partial x_j} + \frac{\partial u_j}{\partial x_i} \right] \right) + \frac{\partial}{\partial x_j} (-\rho_m \overline{u'_i u'_j}) + \rho_m g_j + F_j \quad (2)$$

where u_i and u'_i are the Reynolds-averaged (mean) and fluctuating velocity components, respectively, in the x_i direction, P is the mean pressure, g_j is the acceleration due to gravity, F_j is the body forces arising from the centrifugal and Coriolis forces, ρ_m and μ_m are the volume-weighted mixture density and viscosity respectively. In order to close equation (2), the Reynolds stresses, $-\rho_m \overline{u'_i u'_j}$, need to be modelled. This is done through the use of an eddy-viscosity based turbulence model and a second-moment closure, as described below.

The free-surface of the liquid was modelled using the VoF method.⁴¹ This technique can capture the interfaces between two or more immiscible fluids by tracking the volume fraction of each fluid throughout the computation domain. The tracking of the interface between the phases is accomplished by the solution of a continuity equation for the volume fraction (α) of one of the phases. For the q_{th} phase, the volume fraction equation in the absence of any source term and mass transfer between phases has the following form:

$$\frac{\partial}{\partial t}(\alpha_q \rho_q) + \frac{\partial}{\partial x_i}(\rho_q \alpha_q u_i) = 0 \quad (3)$$

For the homogeneous multiphase system consisting of air and water the above equation is solved for the volume fraction of water (α_w). The volume fraction of air (α_a) can be obtained from the following equation:

$$\alpha_w + \alpha_a = 1 \quad (4)$$

In a given computational cell, $\alpha_w = 1$ represents the cell is full of water, whilst $\alpha_w = 0$ represents the cell only contains air. The air-water interface is determined by identifying the cells where the volume fraction of water is $0 < \alpha_w < 1$.

2.2 Turbulence Modelling. The RST model, which is based on the modelled differential equations for the transport of individual Reynolds stresses, is used here. Calculations were also performed with the SST model of Menter,⁴² which combines the k - ω turbulence model

of Wilcox⁴³ in the near-wall region with the standard k - ε model away from the wall. The performances of these two turbulence models were assessed in this work. Following our previous studies^{13,26}, the standard SST model without streamline curvature correction was used. Previous modelling studies^{44,45} of flow in agitated vessels revealed that no substantial improvement in the predicted mean velocities and turbulence quantities throughout the vessel was achieved using curvature corrected k - ε , k - ω or SST models. Another turbulence modelling approach available in ANSYS-Fluent is the Shear Stress Transport - Scale Adaptive Simulation (SST-SAS) method⁴⁶. In this approach an extra production term is added to the ω -equation which is based on the ratio of turbulent length scale to the von Karman length scale and is only significant in regions of high strain and unsteadiness. Previous studies^{45,47} have revealed that the SST-SAS model predicted mean velocities and turbulence kinetic energy are similar to the k - ε and SST models, moreover the computation time is much higher than these models. This led us not to test the SAS-SST model in this study.

The Reynolds stress transport equations can be expressed in a general form as:

$$\begin{aligned} \frac{\partial}{\partial t}(\rho_m \overline{u'_i u'_j}) + \frac{\partial}{\partial x_k}(u_k \rho_m \overline{u'_i u'_j}) \\ = \frac{\partial}{\partial x_k} \left[\left(\mu + \frac{C_\mu}{\sigma_k} \rho_m \frac{k^2}{\varepsilon} \right) \frac{\partial}{\partial x_k} (\overline{u'_i u'_j}) \right] + P_{ij} + G_{ij} + \phi_{ij} - \rho \varepsilon_{ij} \end{aligned} \quad (5)$$

where P_{ij} is the stress production term and G_{ij} is an additional production term due to the system rotation, both of which are expressed by equations that do not require modelling; however ϕ_{ij} and ε_{ij} , the pressure-strain redistribution and viscous dissipation rate respectively, need to be modelled to close equation (5), and $C_\mu (= 0.09)$ and $\sigma_k (= 0.82)$ are the model constants. The turbulent diffusive transport term (the first term on the right hand side of eq. (5)) is modelled via the generalised gradient-diffusion approach of Daly and Harlow.⁴⁸ The pressure-strain redistribution term (ϕ_{ij}) can be represented either through a linear or a quadratic model. The linear pressure-strain model with a wall-reflection term proposed by Launder, Reece and Rodi⁴⁹ (referred to as the

LLR model) was used in this study. In our previous study²⁶, both the linear LLR model and the quadratic model of Speziale, Sarker, and Gatski⁵⁰ (known as the SSG model) were investigated in simulating flows in an unbaffled agitated vessel and it was found that both models produced similar predictions.

The stress dissipation tensor ε_{ij} is assumed to be isotropic and is modelled in terms of the rate of dissipation of turbulence kinetic energy (ε) as:

$$\varepsilon_{ij} = \frac{2}{3} \delta_{ij}(\varepsilon) \quad (6)$$

where δ_{ij} is the Dirac delta function. The scalar energy dissipation rate (ε) is computed via a modelled transport equation similar to that used in the standard k - ε turbulence model. The turbulence kinetic energy is calculated directly from the normal stresses, which is given by:

$$k = \frac{\overline{u'_i u'_i}}{2} \quad (7)$$

Scalable wall functions were used in the near-wall regions. The application of these functions forces the use of the log-law in conjunction with the standard wall functions approach by introducing a limiter in the grid refinement (y^*) such that

$$y^* = \text{MAX}(y^*, y^*_{\text{limit}}) \quad (8)$$

where $y^*_{\text{limit}} = 11.225$

2.3 Boundary Conditions and Numerical Solution Method. The computational domain illustrated in Figure 2 is discretized using an unstructured mesh. The Reynolds-averaged conservation equations and the transport equations for Reynolds stresses are discretized using the finite-volume discretization method.³⁴ A high-resolution scheme,⁵¹ which is a blend of the first-order and second-order upwind schemes, is used for the discretization of the convection terms in order to reduce the numerical diffusion errors. For the solution of the volume fraction equation (Eq. 3), an interface compressive differencing scheme⁵² and a surface sharpening algorithm⁴¹ are used to provide a greater resolution of the free-surface profile by significantly reducing numerical

diffusion. The discretization of the transient term was carried out using the first-order implicit method.

The no-slip boundary condition together with appropriate wall functions was applied to all the solid surfaces in contact with the fluid. A zero-shear boundary condition was applied at the top of the computational domain which is located at a height of $1.25T$ which provides 25% free space (with air at atmospheric pressure) in order to capture the air-water interface. For simulations using the VoF method, the initial volume fractions of air and water are set to 1 and 0, respectively, in the region above the initial stationary liquid height (i.e., between $1T$ and $1.25T$) and the corresponding volume fractions are 0 and 1 below the air-water interface. The discretized governing equations and the pressure correction equation together with the boundary conditions were solved iteratively with the SIMPLE algorithm to ensure stability and convergence using the ANSYS Fluent-V17.1 CFD code.⁵²

3. CRYSTALLISER CONFIGURATION AND EXPERIMENTAL DETAILS

Hydrodynamic experiments were carried out by Li et al.³¹ as part of our previous research project⁵³ in a 20 L dish-bottom crystalliser with a single cylindrical baffle agitated by a three-bladed RCI representing a typical pharmaceutical crystalliser, as illustrated in Figure 2. These experiments were simulated in the present study. Water was used as the working fluid. The vessel diameter (T) was 294 mm whilst the stationary liquid height was set to $1T$. In order to capture the vortex profile the vessel height (H) was set to $1.25T$. The impeller diameter (D) was 180 mm (with a $D/T = 0.61$), the shaft diameter was 6 mm, and the impeller off-bottom clearance (C) was set to 33 mm (with a $C/T = 0.11$). A single cylindrical baffle with a diameter of 48 mm and length 183 mm was used to mimic a beavertail baffle employed in industrial glass-lined reactors. The dimensions for the vessel are given in Table 1.

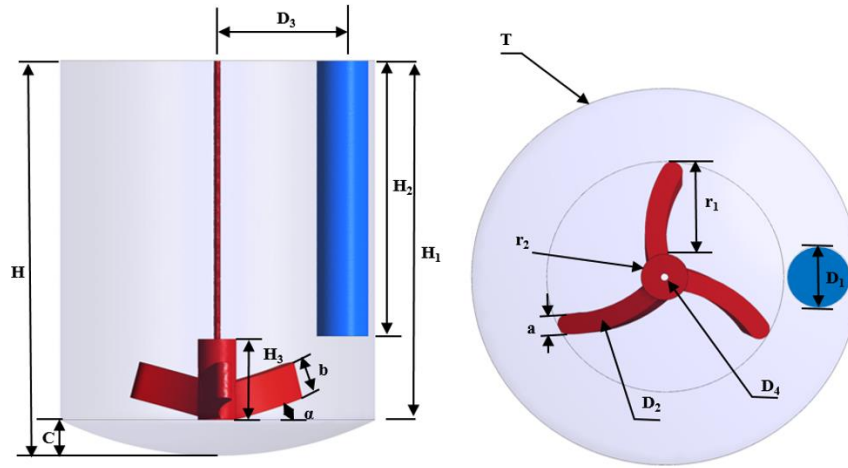


Figure 2. Configuration of the crystalliser with a RCI and a cylindrical baffle.³¹

Table 1. Dimensions of Crystalliser Vessel, Baffle and Impeller (in mm)[†]

H	367	H_1	334	H_2	183
H_3	75	T	294	D_1	48
D_2	36	D_3	120	D_4	6
r_1	90	r_2	86	α	15°
a	16	b	34	C	33

[†]Nomenclature as in Figure 2

In the experiments (see, for details, in Li et al.³¹), a Laser Doppler Anemometry (LDA) was used to obtain phase-averaged measurements of velocity over an entire revolution of the impeller. All the validated Doppler signals arriving over 360° of impeller rotation were accepted and the mean and root-mean-square (rms) velocities were calculated. Measurements were performed at three different impeller speeds of 80, 100 and 150 rpm corresponding to $Re (= \rho ND^2/\mu, N$ is the impeller rotational speed and μ is the viscosity) of 4.3×10^4 , 5.4×10^4 and 8.1×10^4 . The mean velocity components were measured at selected vertical planes located at 15°, 60°, 120° and 180° angular positions relative to the baffle and on each vertical plane nine different heights were selected as illustrated in Figure 3. The reported measurement error was approximately 1% of the impeller tip velocity ($V_{tip} = \pi DN$) with larger errors, 2–3% of V_{tip} , in regions close to the impeller and of steep velocity gradients. Measurements performed in an un baffled vessel

agitated by a Rushton turbine using the same LDA system by Liang³³ (also see Haque et al.²⁶) reported that the errors in the mean and rms velocities were 1–3% and 5–10% of V_{tip} , respectively, with larger errors observed in the regions of steep velocity gradients.

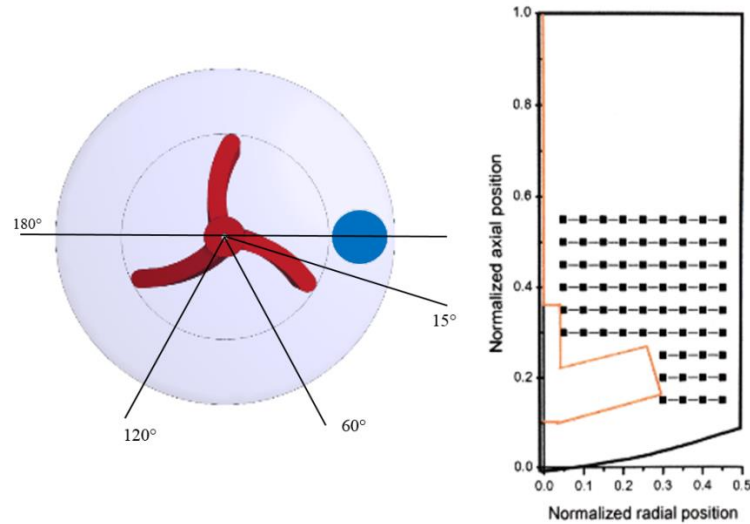


Figure 3. Angular and vertical locations for velocity measurements.³¹

4. APPLICATION OF CFD MODELLING METHODOLOGY

4.1 Computational Details. The three-dimensional transient flow simulations were performed using the sliding-mesh technique.⁵⁴ In order to apply this procedure, the mesh was divided into two parts: an inner rotating mesh covering a cylindrical volume enclosing the impeller and its shaft and an outer stationary mesh which covered the rest of the vessel including the baffle, with the rotating mesh sliding relative to the stationary mesh. The location of the interface between the two meshes was set at the middle of the gap between impeller tip and the baffle to ensure that the region of flow periodicity associated with the impeller motion was contained within the rotating mesh. An unstructured computational mesh was used which consisted of 6×10^5 elements with smooth transition to inflated boundaries comprising prismatic elements to resolve the boundary layer along the solid surfaces and tetrahedral elements covering the rest of the domain. A uniform mesh was used throughout the domain except in the proximity of the solid surfaces and

in the region below the impeller shaft that extends up to the lowest point of the vessel's torispherical bottom. Figure 4 illustrates the computational mesh used in the simulations. Although the initial level of the water in the vessel was $1T$, the height of the computational domain was extended to $1.25T$ in order to capture the air-water interface for those simulations in which the free-surface was modelled using the VoF approach. Mesh independence tests were carried out in our previous work.³¹ Three mesh sizes consisting of 1.7×10^5 (coarse), 2.7×10^5 (medium) and 4.0×10^5 (fine) elements were used which revealed that both the medium and fine meshes were sufficient to obtain acceptable mesh independent flow predictions. It should be noted that the mesh used in this study has more cells than the fine mesh employed by Li et al.³¹ thus further ensuring mesh independence of the predictions.

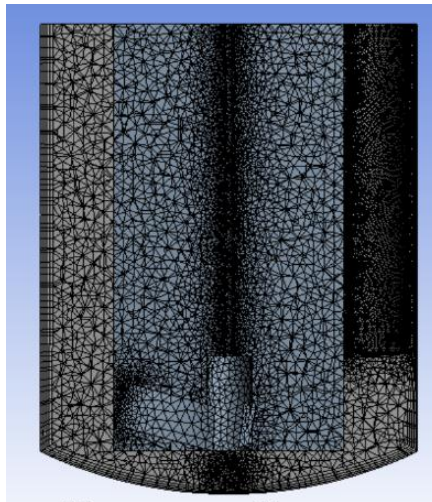


Figure 4. Computational mesh for the crystalliser.

To provide initial values for the transient simulation for a given impeller speed, a steady-state simulation was first performed using the frozen rotor frame model for flat liquid surface with the SST turbulence model. 500 iterations were sufficient for the residual to fall below the target value of 10^{-5} . The transient flow computation with the sliding mesh technique together with the RST model was initiated with the corresponding steady-state simulation results. The calculation was carried out until the completion of at least nine impeller revolutions with a time step of 0.005

s after which the solution reached a periodic steady-state associated with the movement of the impeller blades as previously demonstrated in our previous publication.³¹ After selecting the VoF option among the available multi-phase models, eight additional impeller revolutions were simulated to ensure that the vortex profile became invariant. Target residuals were set to 10^{-5} with 20 iterations per time step being adequate for these to fall below the target. The simulations were run on a Intel(R) Xeon(R) CPU E5-278W v4 workstation @ 3.00 GHz (2 processors) with 128 GB memory under the Windows 2012 operating system. A typical run time was 8 h using the RST model. Imbalances in the overall mass and momentum conservation at the end of a typical simulation were below 0.5% for the target residual.

Simulations were performed for two different impeller speeds 100 and 150 rpm corresponding to Re of 5.4×10^4 and 8.1×10^4 . This paper presents representative simulation results of the mean velocity components, averaged over one complete rotation (360°) of the impeller, and comparisons with those obtained experimentally on the 60° and 180° planes for 100 rpm and on the 180° plane for 150 rpm at four different heights in each plane. The predicted and measured turbulence kinetic energy are compared on the 180° plane for 100 rpm.

4.2 Hydrodynamic Macro-parameters. With the aim of assessing the effect of fluid properties and impeller speed on the hydrodynamics macro-parameters and vortex depth, simulations were carried out by varying the impeller speed between 100 and 250 rpm and the viscosity of the liquid within the range of 1.00×10^{-3} and 6.01×10^{-2} Pa s. The viscosity of the liquid was varied by mixing 20–80 wt. % glycerol with water. The crystalliser macro-mixing performance was assessed through the estimation of: impeller power number, impeller flow number and secondary circulation flow number which were calculated using the predicted mean velocity distributions.

The power number (N_p) defined by equation (9) can be calculated using the power consumption (P) in the vessel given by equation (10):

$$N_p = \frac{P}{\rho N^3 D^5} \quad (9)$$

$$P = \omega \int_A \mathbf{r} \times (\boldsymbol{\tau} dA) \quad (10)$$

where N is the impeller rotational speed, D is the impeller diameter, ω is the angular velocity, \mathbf{r} is the position vector, $\boldsymbol{\tau}$ is the stress tensor and A is the overall impeller and shaft surface area.

The flow discharged from the impeller can be represented by the dimensionless impeller flow number (N_d) given by:

$$N_d = \frac{w_d}{\rho N D^3} \quad (11)$$

In this, the flow that crosses the impeller plane known as pumping capacity (w_d) was estimated using equation (12). Because the RCI acts largely as a radial-flow impeller, the impeller flow can be calculated by integrating the radial component of the mean velocity (v_r) over a cylindrical surface coaxial with the impeller enclosing the blades:

$$w_d = \int_{z_b}^{z_t} 2\pi\rho R_b v_r dz \quad (12)$$

where R_b is the radius of the cylindrical surface located at the mid-point between the impeller blade tip and the inside edge of the baffle, z_b and z_t are the impeller blade bottom and top height, respectively.

The secondary circulation flow number (N_c), given by equation (13), characterises the convective mixing within the tank and is defined as the axial flow directed upwards (w_{up}) across a reference plane normal to the impeller shaft covering the whole cross-section of the tank and it is located at a height z_t .

$$N_c = \frac{w_{up}}{\rho N D^3} \quad (13)$$

$$w_{up} = \int_{A^+} \rho v_z dA_z \quad (14)$$

5. RESULTS AND DISCUSSION

5.1 Flow Patterns. The predicted flow patterns and the distributions of turbulence kinetic energy and energy dissipation rate on a vertical plane at the 0-180° angular position (see Figure 3) for impeller speeds of 100 and 150 rpm are displayed in Figures 5 and 6, respectively. The corresponding flow patterns at three selected horizontal planes perpendicular to the impeller shaft are also illustrated in Figures 7 and 8. These predictions were obtained using the RST turbulence model together with VoF for capturing the liquid free surface profiles.

As can be observed in Figures 5 and 6, on the left side of the impeller shaft flow discharges from the impeller blade tip in the radial direction which impinges on the vessel wall, producing a flow structure similar to that of a wall jet. After impingement, the liquid flows along the wall vertically up and downwards towards the bottom of the vessel. The liquid from the top is drawn down around the impeller shaft. The flow structure in the proximity of the wall reveals the formation of secondary vortices in the region above the impeller. On the right side of the impeller shaft, the radial flow impinges on the bottom of the cylindrical baffle forming a recirculation zone. Unlike in the vessels fitted with wall-mounted flat baffles, the upward flow decays rapidly before reaching the top of the vessel with decreasing magnitude of the axial velocity with increasing distance from the impeller, resulting in poorly agitated regions near the liquid surface.

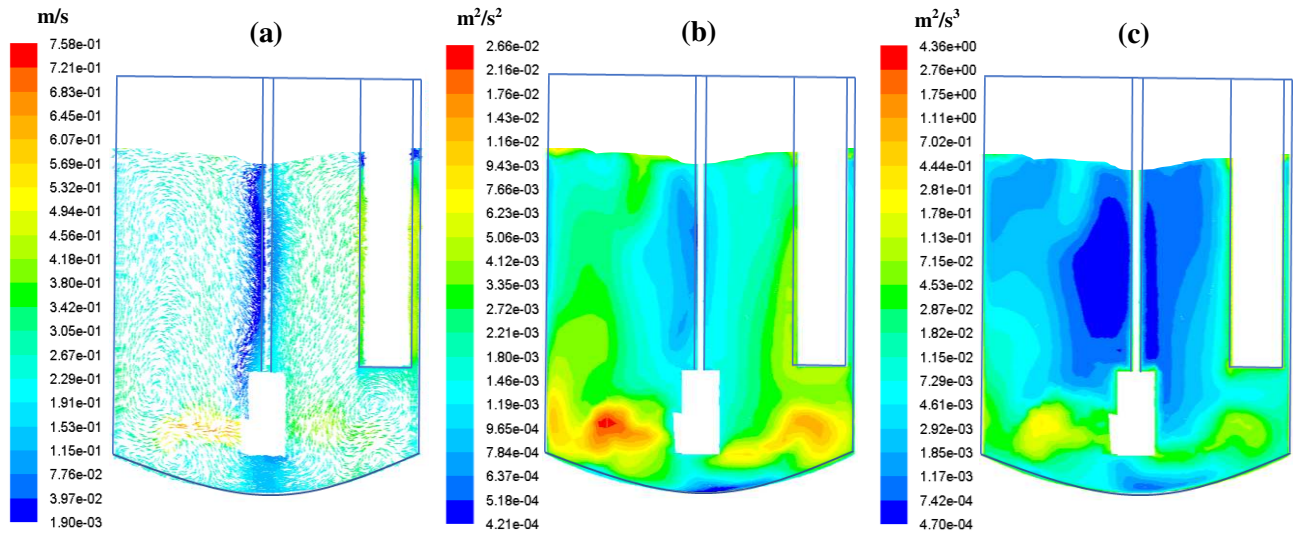


Figure 5. Predicted (a) flow pattern and distributions of (b) turbulence kinetic energy (k) and (c) energy dissipation rate (ε) for 100 rpm at the 0–180° plane (contours of k and ε are in logarithmic scale) after 38.62 s.

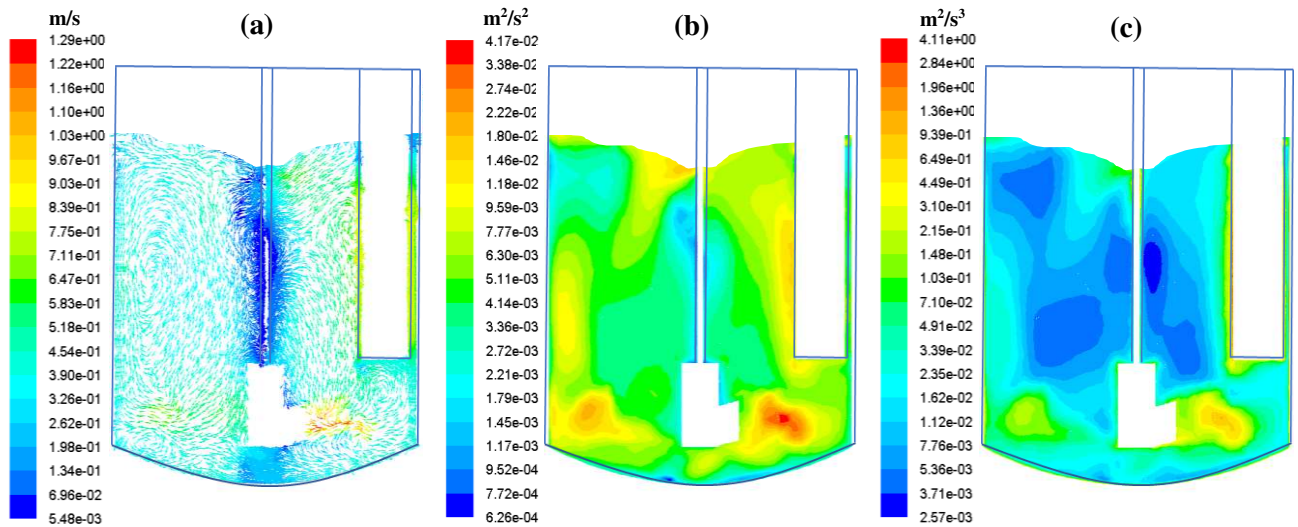


Figure 6. Predicted (a) flow pattern and distributions of (b) turbulence kinetic energy (k) and (c) energy dissipation rate (ε) for 150 rpm at the 0–180° plane (contours of k and ε are in logarithmic scale) after 31.6 s.

The flow patterns in terms of rotational velocity vectors on three horizontal plans passing through the bottom, middle and near the top of the baffle for 100 and 150 rpm are displayed in Figures 7 and 8, respectively. A strong swirling flow exists at the bottom of the baffle (Figures 7a

and 8a) and in the region below with a high tangential velocity along the wall. At higher planes, the swirling flow is impeded by the presence of the baffle as shown in Figures 7b,c and 8b,c. The flow patterns on these two planes reveal formation of vortices behind the cylindrical baffle which resemble flow past a circular cylinder. As expected, an overall higher swirl intensity can be observed in the predictions for 150 rpm in Figure 8.

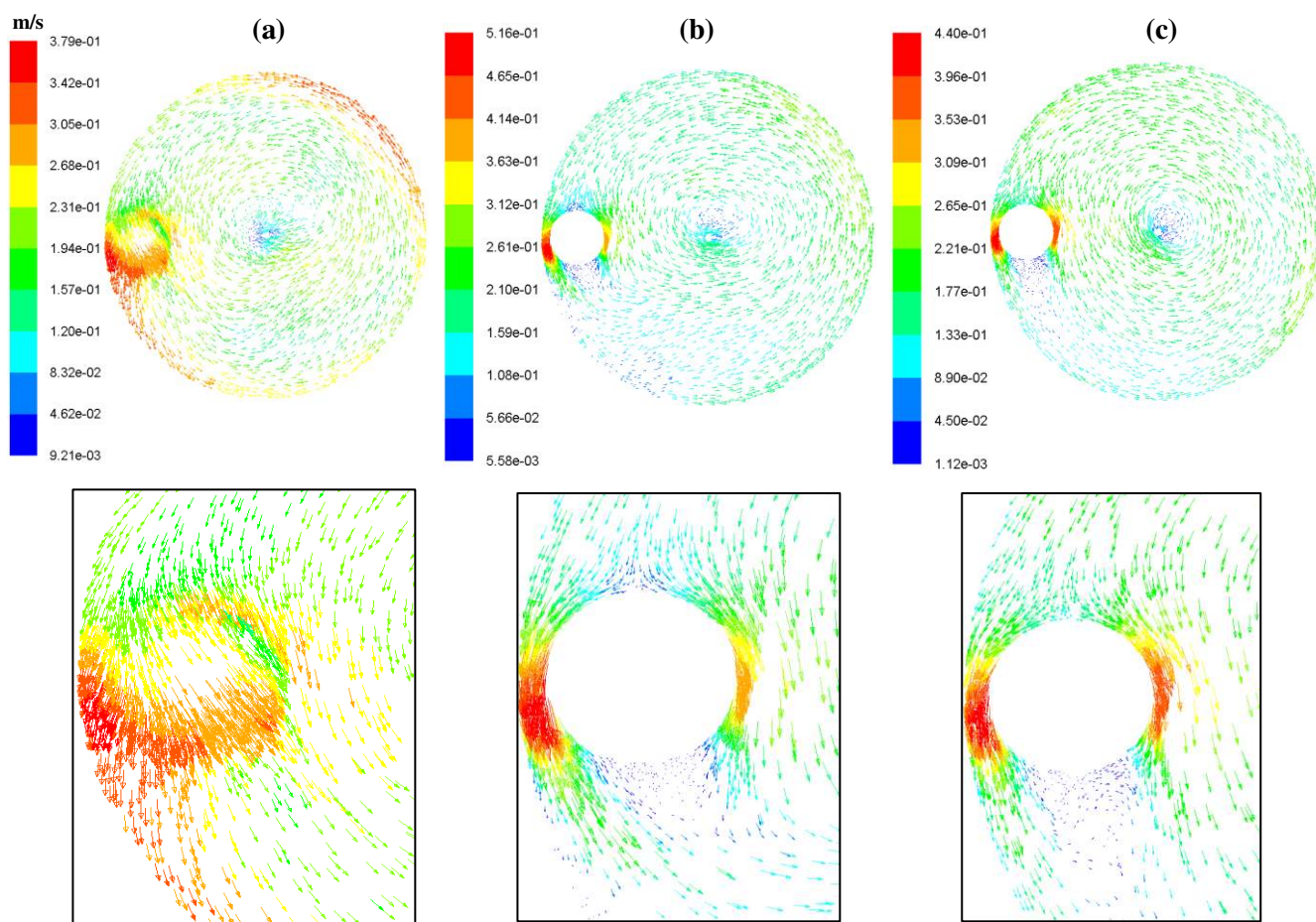


Figure 7. Predicted flow patterns on three horizontal planes above the impeller for 100 rpm ((a) just below the bottom, (b) middle and (c) near the top of the baffle according to Figure 5).

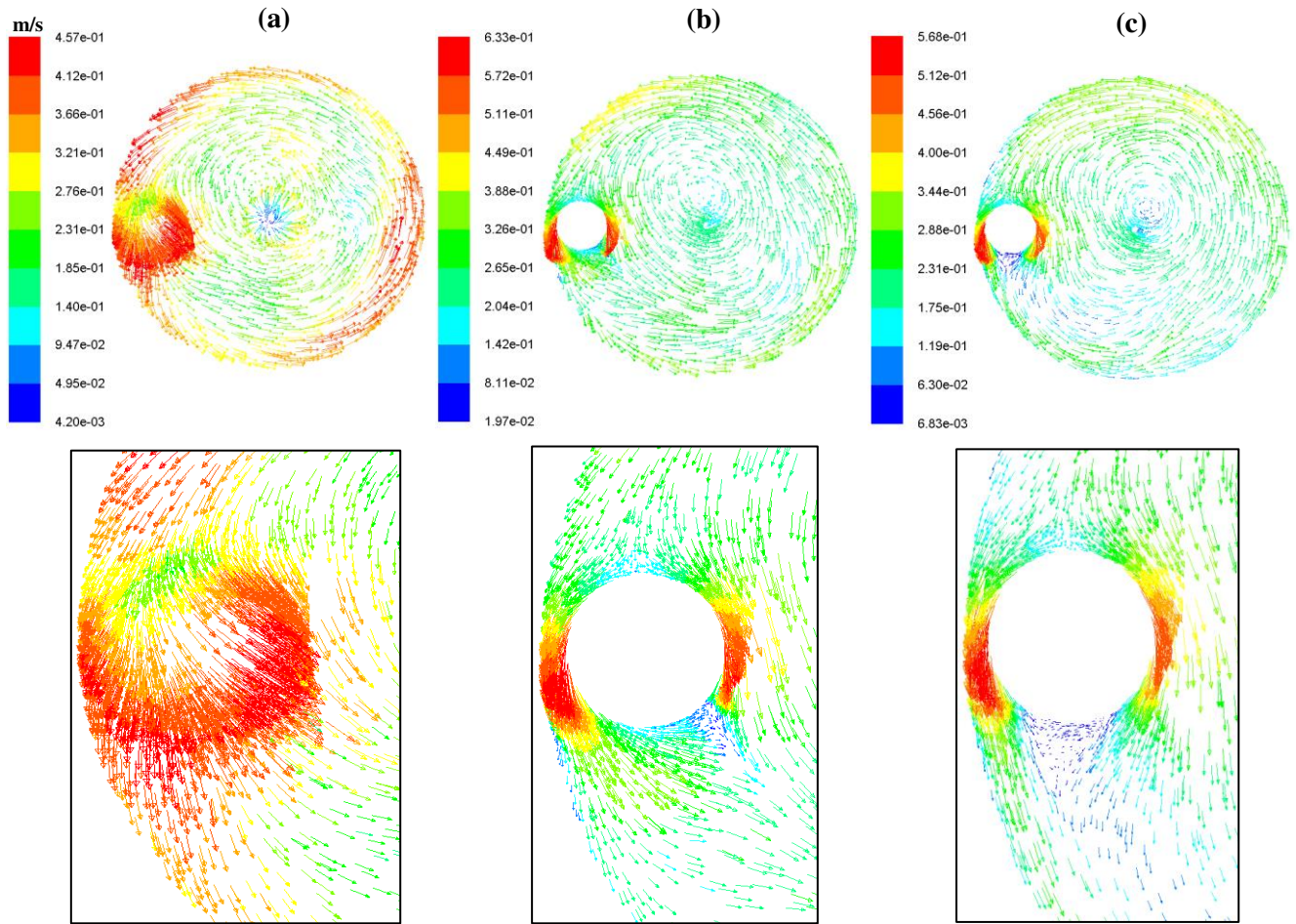


Figure 8. Predicted flow patterns on three horizontal planes above the impeller for 150 rpm ((a) just below the bottom, (b) middle and (c) near the top of the baffle).

The distributions of turbulence kinetic energy (k) and energy dissipation rate (ε) illustrated in Figures 5b,c and 6b,c reveal that both the turbulence parameters vary significantly, by two to three orders of magnitude, through the vessel which is more pronounced for the energy dissipation rate. High values of both k and ε occur in the impeller stream, in the proximity of the baffle and in the upward flow along the wall, with the highest being in the vicinity of the blades which decrease in the region away from the impeller. This is due to large spatial velocity gradients in these regions compared with those in the bulk flow. As the impeller speed increases higher values of these parameters are observed in Figure 6 notably within the impeller blades region.

Overall, the gross flow patterns and the distributions of turbulence kinetic energy and energy dissipation rate predicted with and without VoF (i.e. for flat liquid surface) are qualitatively similar in the region away from the liquid surface.

5.2 Comparison of CFD Predictions with LDA Data. A number of flow simulations were carried out using the SST and RST turbulence models with flat liquid surface and with the VoF for capturing free-surface vortex formation. The simulation results reveal that improved predictions are achieved using the RST model coupled with the VoF compared with those using the SST model and with a flat liquid surface as used in the previous study.³¹ Figure 9 shows comparisons between the predicted mean velocity components using both the RST and SST turbulence models with VoF and experimental data for 100 rpm on the 180° plane. Although the SST model predictions compare reasonably well with the experimental data, better predictions for the axial and radial velocities are observed when the RST turbulence model is used.

Comparisons between the predicted mean axial, radial and tangential velocities using the RST turbulence model for both flat and free-liquid surface (capturing surface profile) and experimental data for 100 and 150 rpm are displayed at representative angular positions (60° and 180°) and at four heights in Figures 10-12. As can be seen, the predicted velocities obtained with the VoF method are generally in better agreement with the experimental data than those for the flat liquid surface. At the measurement locations above the impeller, the RST-VoF model correctly predicts the shape of the measured tangential velocity profiles which conform to that of a combined vortex consisting of an inner region of forced-vortex motion (or solid-body rotation) and an outer region of free-vortex motion. Whereas, the RST model without VoF erroneously predicts forced-vortex profiles and as a consequence the tangential velocity is significantly underpredicted in the inner region of the flow. The predicted axial velocity distributions using the RST-VoF model in the upward-directed flow along the wall and in the recirculation zone are in much better agreement with measurements compared with those predicted by the RST model without VoF. The latter

approach predicts a very strong recirculating flow particularly at 150 rpm. The width of the upward-directed flow is correctly predicted by the RST-VoF model. The radial velocities along the impeller stream predicted by both modelling approaches agree very well with the measurements. However, discrepancies exist between the measurements and predictions in the region above the impeller. In this region, the RST-VoF model provides better predictions of the radial velocity distributions as can be observed at the 180° plane for 100 and 150 rpm in Figures 11 and 12. However, both modelling approaches underpredict the radial velocity particularly in the recirculation zone at the 60° plane for 100 rpm (Figure 10). Comparisons between the predicted and measured mean velocity components illustrated in Figures 10-12 emphasise that an accurate representation of the liquid free-surface profile is essential for achieving an improved prediction of the flow field in partially baffled vessels.

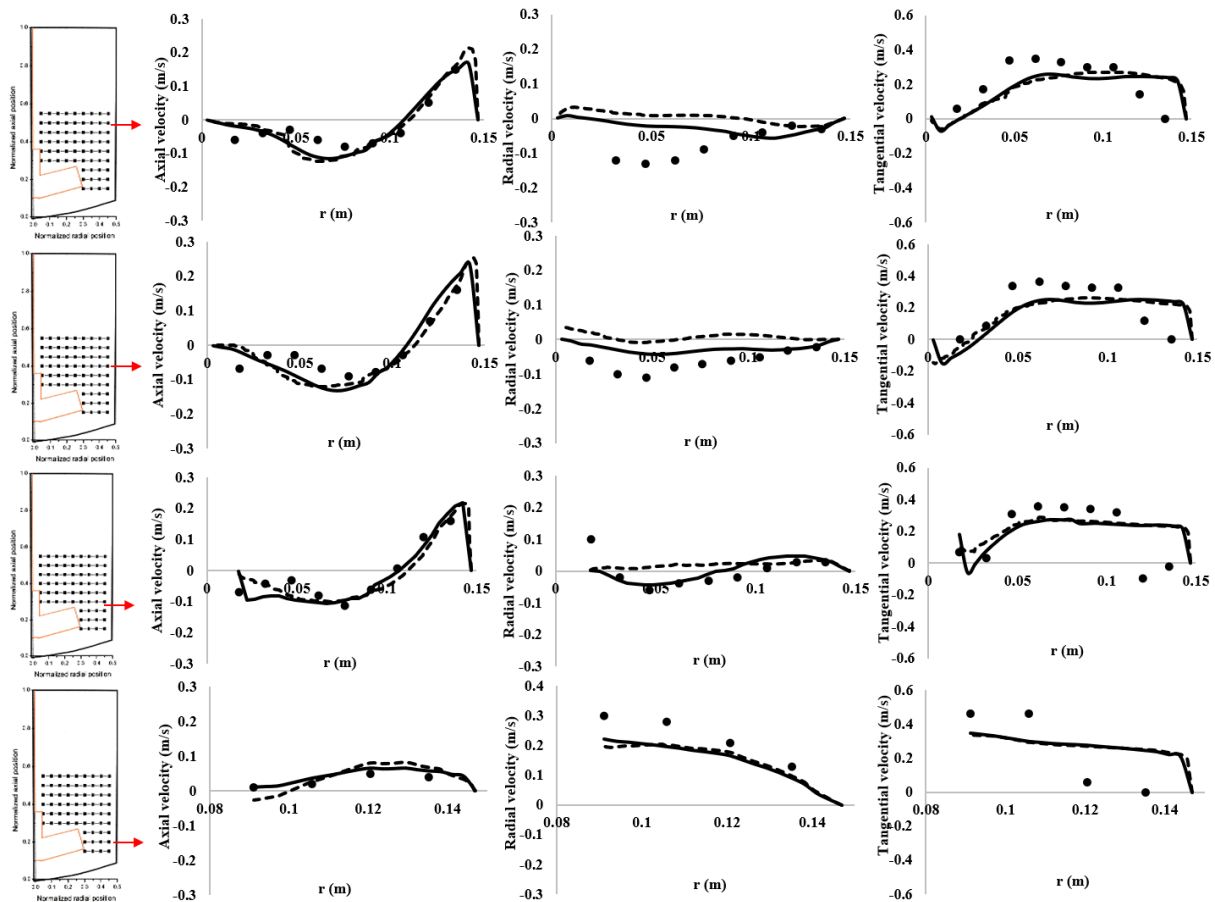


Figure 9. Predicted and measured mean velocity components at 100 rpm at four selected heights on the 180° plane: (●) LDA data,³¹ RST with VoF (—) and SST with VoF (---).

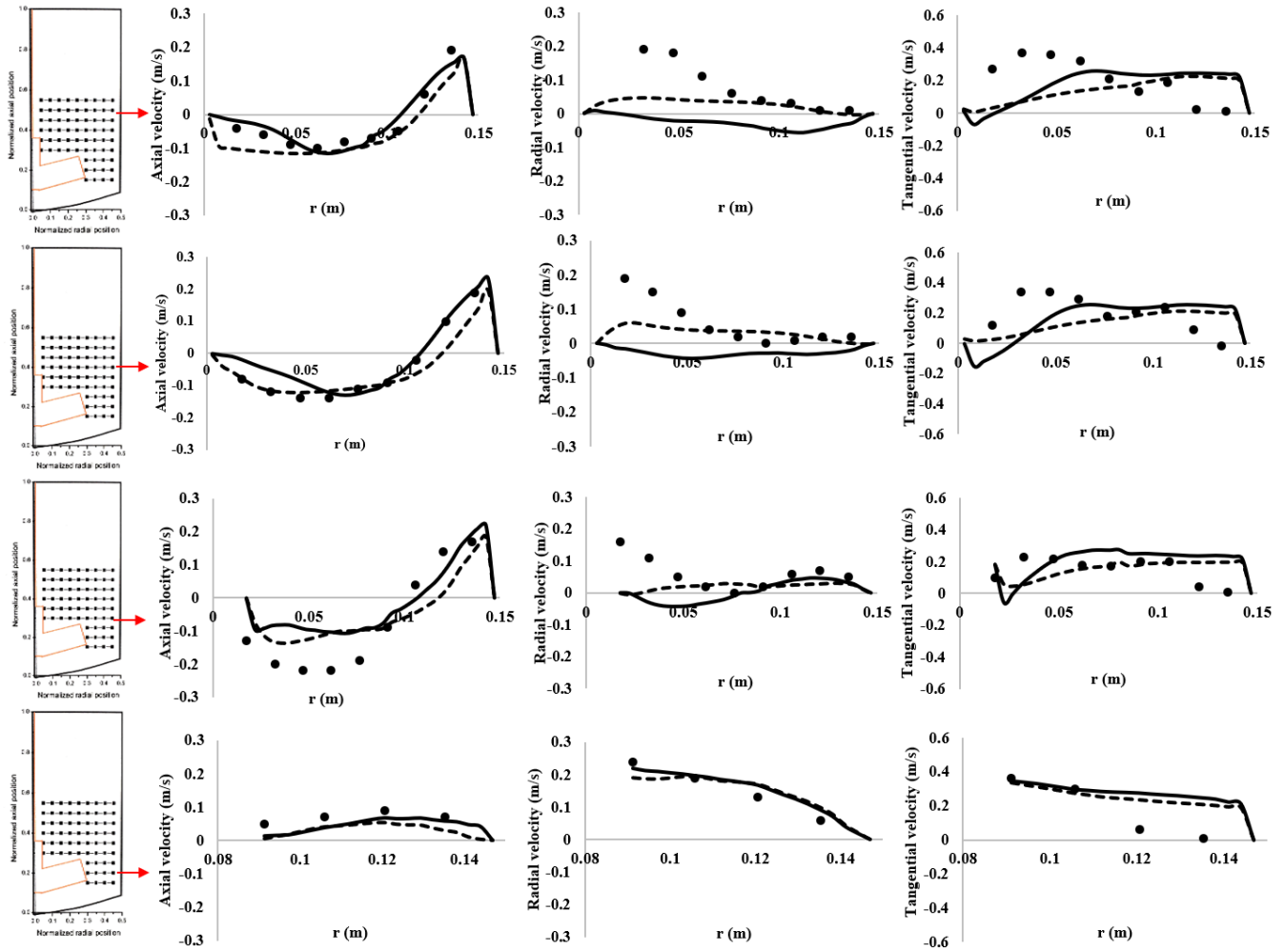


Figure 10. Predicted and measured mean velocity components at 100 rpm at four selected heights on the 60° plane: (●) LDA data,³¹ CFD with VoF (—) and with flat liquid surface (----).

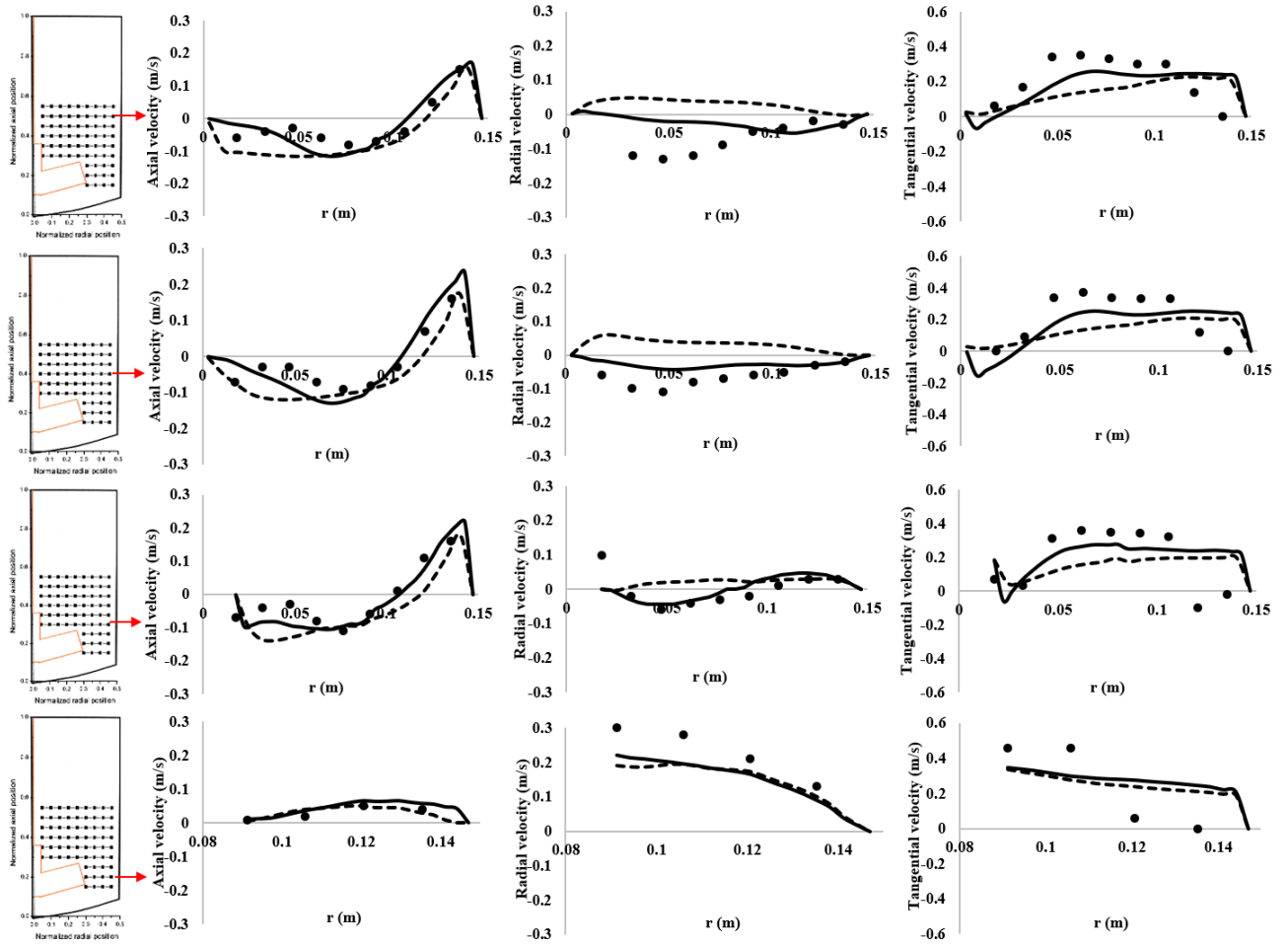


Figure 11. Predicted and measured mean velocity components at 100 rpm at four selected heights on the 180° plane: (●) LDA data,³¹ CFD with VoF (—) and with flat liquid surface (----).

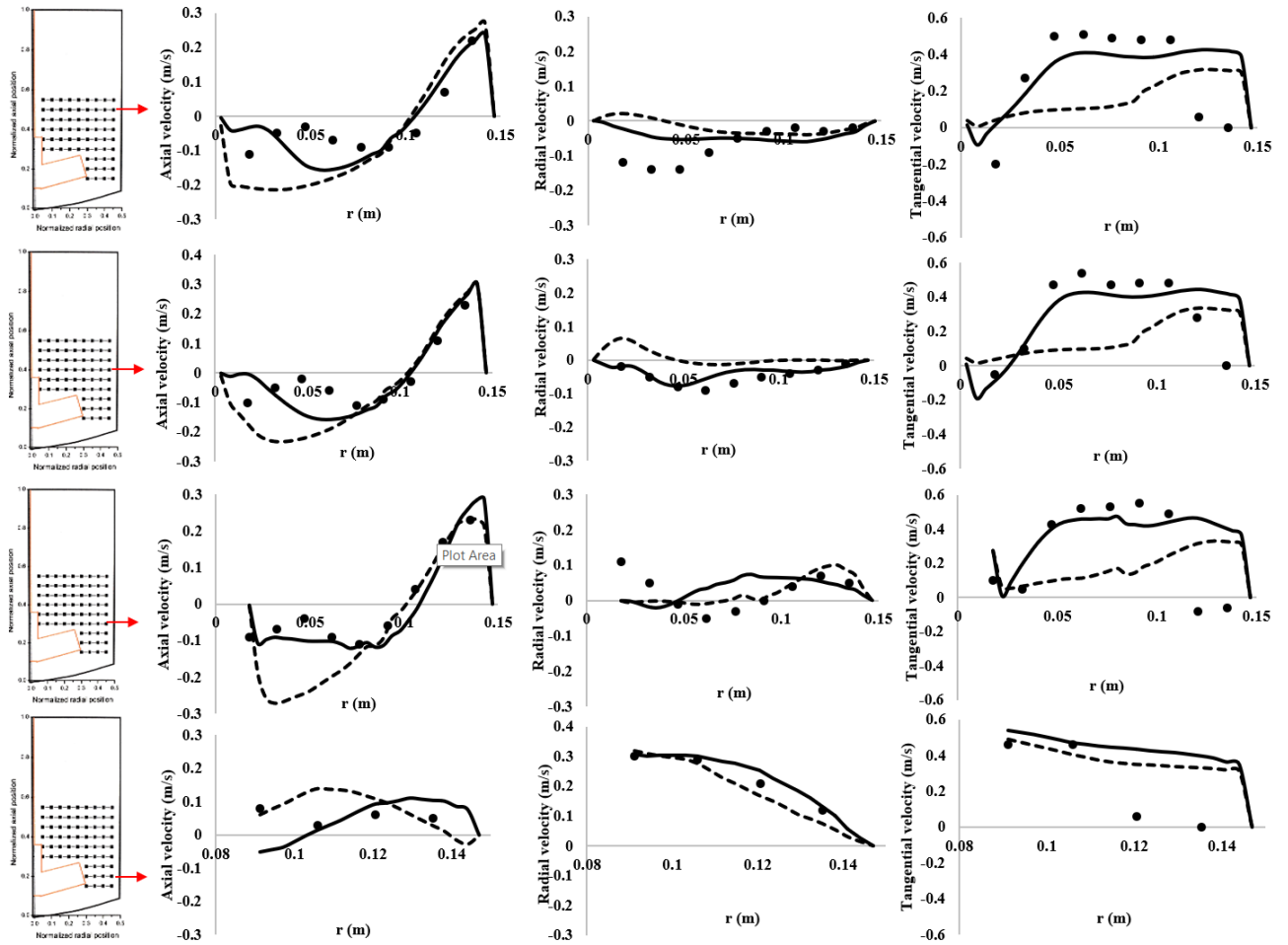


Figure 12. Predicted and measured mean velocity components at 150 rpm at four selected heights on the 180° plane: (●) LDA data,³¹ CFD with VoF (—) and with flat liquid surface (----).

Figure 13 illustrates the CFD predicted radial profiles of the turbulence kinetic energy in comparison with the random part of turbulence kinetic energy obtained from averaging the phase-resolved LDA measurements of rms velocities.³¹ High levels of measured turbulence kinetic energy occur in the impeller stream and in the upward-directed flow near the wall just above the impeller. As can be seen, in these regions the turbulence kinetic energy is significantly underpredicted by both the modelling methods. On the whole, the turbulence kinetic energy is underestimated by one order of magnitude. In the impeller region, the predicted values using the RST model range approximately from 0.002 to $0.005 \text{ m}^2/\text{s}^2$ whilst experimental data range from 0.02 to $0.08 \text{ m}^2/\text{s}^2$. In the bulk of the flow away from the impeller, the predicted values vary from 0.0004 to $0.002 \text{ m}^2/\text{s}^2$ and measured values from 0.01 to $0.02 \text{ m}^2/\text{s}^2$. It should be noted that it was

difficult to amass sufficient quantity of phase-resolved experimental data in order to extract accurately the random part of the turbulence kinetic energy in the impeller region.³¹ The contribution from the periodic velocity fluctuations due to the passage of the impeller blades to the measured turbulence kinetic energy can be significant as found in previous studies (for example, Ng et al.⁵⁵, Montante et al.⁵⁶ and Alcamo et al.⁵⁷). Strictly speaking the CFD predictions of the turbulence kinetic energy can only be compared with measurements in the bulk flow above the impeller where this contribution is small. Therefore, the discrepancies between the measurements and predictions can partly be attributed to this effect together with the errors generally associated with the LDV measurement techniques in the near-impeller region.⁵⁵ However, the deficiencies of the RANS approach as well as that of the RST model, which stems from the modelling of the pressure-strain redistribution term and the stress dissipation rate tensor (ε_{ij}) in equation (5),⁵⁸ cannot be ruled out. It has also been found by Jaworski and Zakrzewska⁵⁹ and Murthy and Joshi³⁷ in baffled agitated vessels that the RST model underperforms in the impeller region.

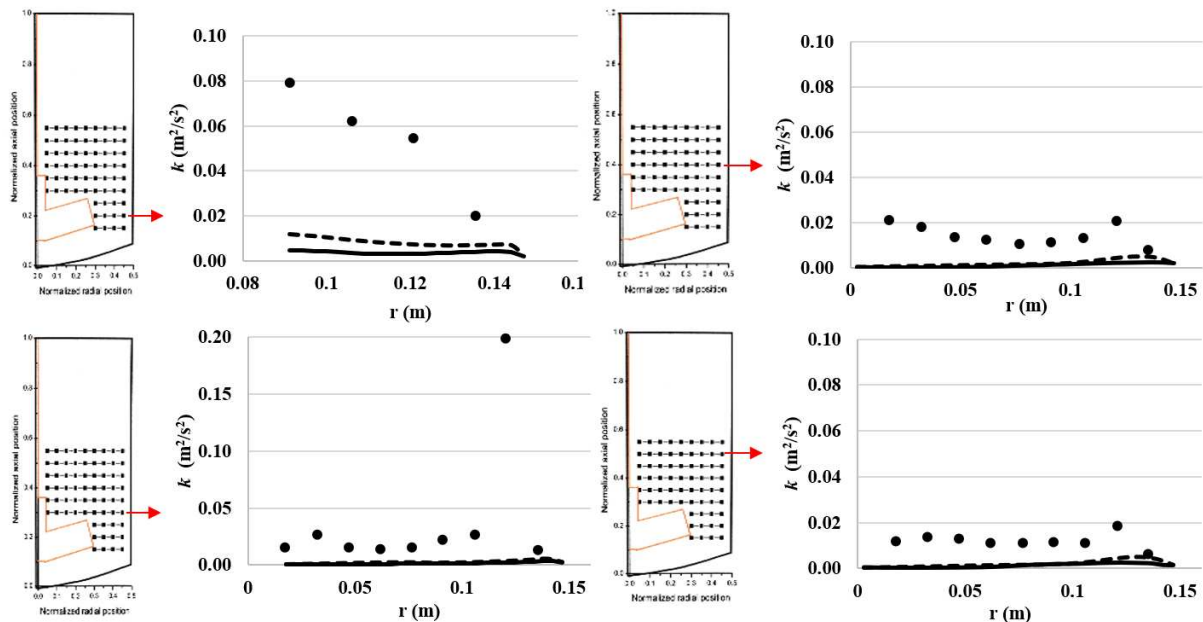


Figure 13. Predicted and measured turbulence kinetic energy at 100 rpm at four selected heights on the 180° plane (●) LDA data,³¹ CFD with VoF (—) and with flat liquid surface (----).

5.3 Effect of Impeller Speed and Liquid Viscosity on Vortex Depth and Hydrodynamic Macro-parameters. Simulations were carried out using water and water-glycerol mixtures as working fluids in order to assess the effect of the impeller speed and the liquid viscosity on vortex formation. A liquid volume fraction of 90% was used to define the air-liquid interface as suggested in previous studies in unbaffled agitated vessels.^{10,22} The predicted instantaneous liquid free-surface profiles of water due to the transient nature of the surface topography on the 90–270° angular position (see Figure 3) for impeller speeds of 100, 150, 200 and 250 rpm are illustrated in Figure 14. As can be seen, a single baffle is unable to suppress vortex formation, particularly at higher impeller speeds (> 100 rpm), and the vortex depth increases with increasing impeller speed. Figure 15 reveals that at a constant impeller speed of 150 rpm, the vortex depth for water-glycerol mixtures decreases with the increase in liquid viscosity (and hence decrease in Re) as the flow regime approaches from fully turbulent towards laminar conditions at higher viscosities.

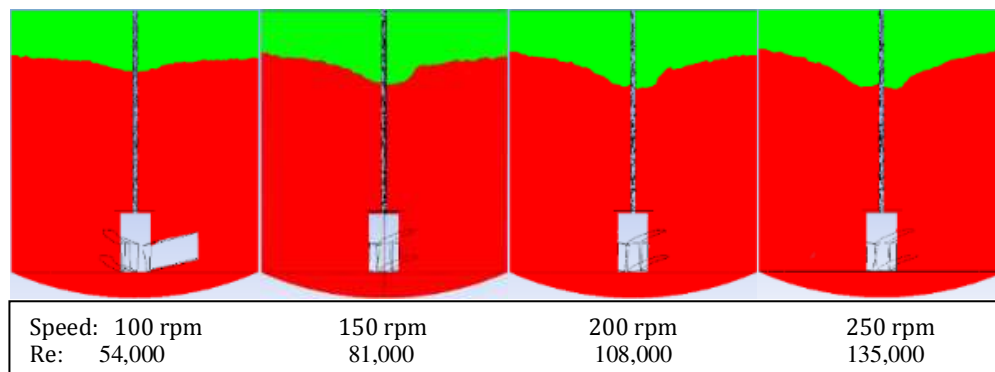


Figure 14. Predicted instantaneous vortex profiles of water as a function of impeller speed on the 90–270° plane.

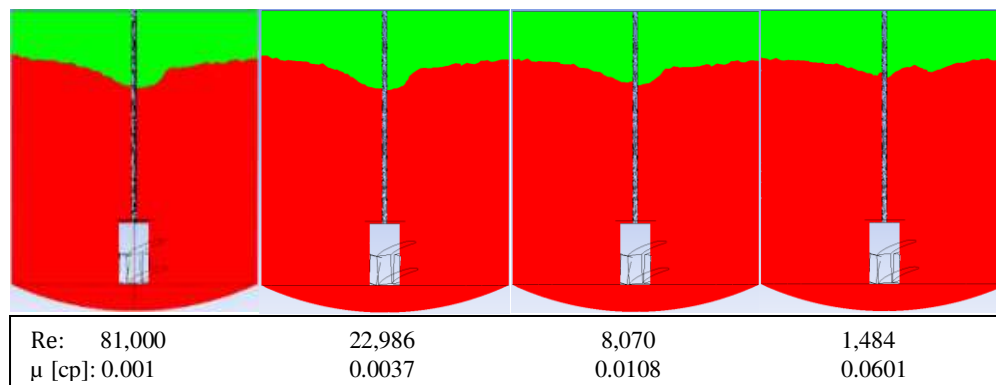


Figure 15. Predicted instantaneous vortex profiles of water-glycerol mixtures as a function of the viscosity at 150 rpm on the 90–270° plane.

Although a depression in the liquid free-surface was experimentally observed in our previous work,³¹ the accuracy of the predicted vortex depth cannot be ascertained quantitatively in the absence of measurements or vortex depth correlations for a single-baffled vessel in the literature. However, Figure 16 illustrates quantitative comparisons between the vortex depths for water in the present crystalliser predicted by the CFD-VoF method and those calculated from Nagata's correlation¹⁵ for unbaffled vessels, a modification to this correlation by Smit and During¹⁶ (see derivation in S1 of the Supporting Information) and Deshpande et al.¹⁸ (see S2) and measured in a reactor with two cylindrical baffles.²⁹ This comparison reveals that the vortex depths without baffles calculated from these correlations are significantly higher than those predicted by CFD for the single-baffled vessel. It is interesting to note that the vortex depths for partially baffled vessels are very close. The effect of baffle on vortex depth can be explained by the fact that the swirling flow in the vessel become less intense and the contributions of the axial and radial velocities become significant as the number of baffle increases.

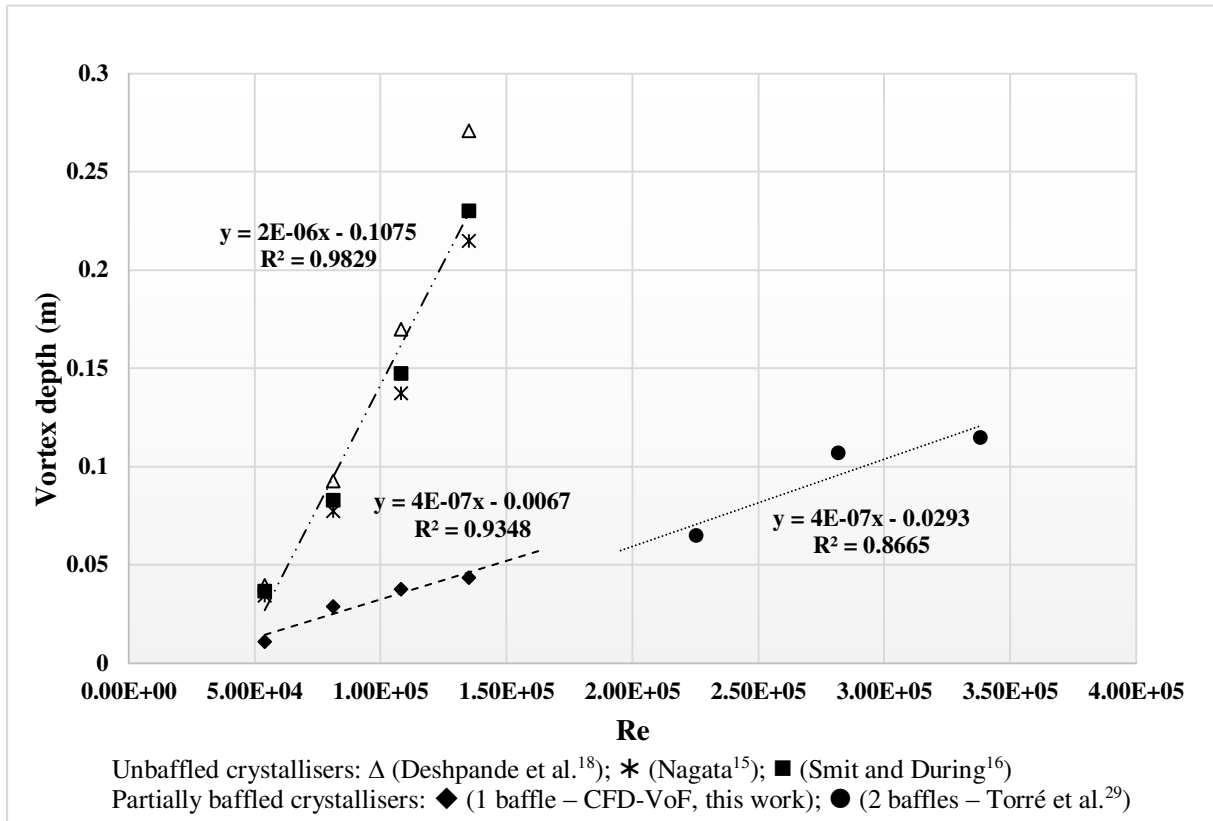


Figure 16. Comparison of vortex depth of water as a function of Re: predicted using CFD-VoF for the present single-baffled vessel, calculated from various correlations developed for un baffled vessels (Nagata¹⁵, Smit and During¹⁶ and Deshpande et al.¹⁸) and experimental data for a twin-baffled vessel (Torr e et al.²⁹). Note: The lines represent trend lines fitting the corresponding data set.

Figure 17 shows the predicted variation of vortex depth as functions of the impeller speed and liquid viscosity expressed in terms of Re. Whilst, as expected, the higher the Re the higher is the vortex depth, the viscous liquid in general exhibits significantly lower vortex depths. For $Re > 2.0 \times 10^4$, the vortex depth increases significantly with Re only for a significant decrease in viscosity (i.e., from 0.0025 to 0.001 cp) while remaining virtually constant for a change in viscosity from 0.0025 to 0.0037 cp for a constant impeller speed.

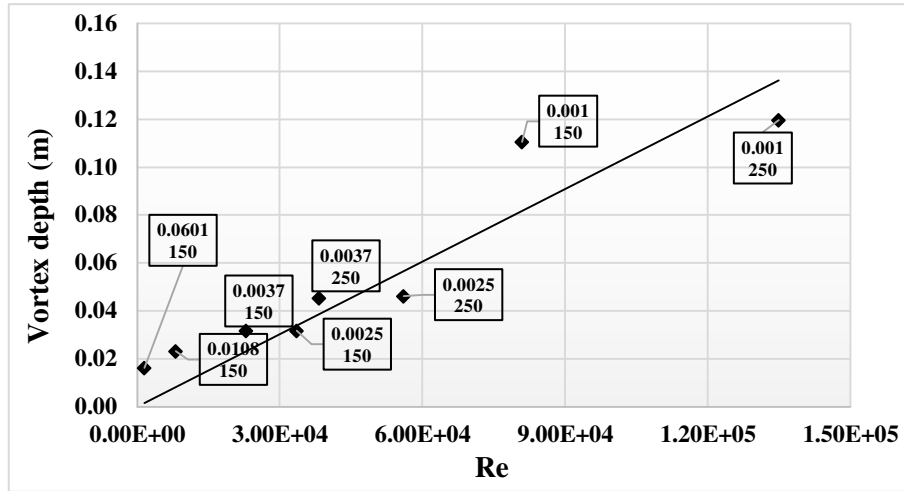


Figure 17. CFD-VoF predicted vortex depth of water-glycerol mixtures as functions of impeller speed and viscosity (Numbers associated with the data points represent the mixture viscosity [cp] (top) and impeller speed [rpm] (bottom). Note: The line represents a trend line fitting the data points.)

The values of power number and impeller flow number for the impeller speeds of 100, 150, 200 and 250 rpm (with corresponding Re values of 5.4×10^4 , 8.1×10^4 , 1.08×10^5 and 1.35×10^5) calculated from CFD-VoF simulation results using water as a working fluid together with published measured data of power number within the Re range of $1 \times 10^4 > \text{Re} > 1 \times 10^6$ are presented in Table 2. Figure 18 depicts the trend of hydrodynamic parameters (N_p , N_d and N_c) as a function of Re. This comprises the results of the entire set of simulations carried out using the properties of both pure water and water-glycerine mixtures in order to assess the effect of both impeller speed and liquid properties on these parameters. It should be noted that flow calculations for $\text{Re} > 1.0 \times 10^4$ were carried out using the RST turbulence model and for $1.5 \times 10^3 < \text{Re} < 1.0 \times 10^4$ the transition SST model of Menter et al.⁶⁰, as implemented with adjusted model constants in ANSYS Fluent, was used; whilst for $\text{Re} < 1.5 \times 10^3$ the laminar flow calculation was invoked, although such flows in agitated vessels exist at a much lower Re. This approach had to be adopted as the transition SST model failed to reach periodic steady-state solutions for $\text{Re} < 1.5 \times 10^3$ even after a large number of simulated impeller revolutions. As can be seen in Table 2, the CFD predicted power numbers are within the range of measured values for the dish-bottom vessels with

a single²¹ and two beavertail baffles^{19,20}, with the exception of reference²² with a single beavertail baffle where the measured N_p is lower than the predicted values, the reason for which is not clear. However, it is worth noting that this value is also lower than those reported in references¹⁹⁻²¹. Rielly et al.²⁴ reported smaller values of N_p for flat and conical bottom vessels with a RCI and a single beavertail baffle of diameter of 0.029 m which can be attributed to the vessel geometry. It is well known that the power number depends on factors such as impeller clearances, baffle number and size, and the shape of the vessel base. Whilst the predicted values of N_p were obtained for a dish-bottom vessel with a single baffle of 0.048 m diameter (with a dimensionless baffle diameter, defined as the ratio of the baffle to vessel diameter, $D_1/T = 0.163$), the measured values in reference²² were obtained for a single baffle of diameter of 0.022 m ($T = 0.450$ m and $D_1/T = 0.049$), and those in references^{19,20} for two beavertail baffles of 0.025 m diameter ($T = 0.308$ m, thus $2D_1/T = 0.162$). It is interesting to note that D_1/T ratios in the present study and in references^{19,20} are almost identical and the N_p values in both cases are very similar as shown in Table 2, whereas the D_1/T ratio in reference²² is approximately one fourth of the other cases resulting in a much lower N_p value of 0.5. An increase in power number should be expected with an increase in baffle number/size due to the shift of flow pattern from a rotational flow to a predominantly vertical recirculating flow.

Table 2. Predicted Power Number (N_p) and Impeller Flow Number (N_c) at different impeller speed using water as a working fluid and comparison with measured N_p .

CFD predicted N_p and N_c				Measured N_p^\dagger
Speed (rpm)	Re	N_p	N_c	
100	5.4×10^4	0.79	0.30	0.70–0.79 ^{19,20} ($1.0 \times 10^4 < \text{Re} < 2.4 \times 10^5$)
150	8.1×10^4	0.70	0.30	0.60–0.80 ²¹ ($1.0 \times 10^4 < \text{Re} < 1.0 \times 10^6$)
200	1.08×10^5	0.70	0.31	~ 0.5 ²² ($1.0 \times 10^4 < \text{Re} < 5.0 \times 10^5$)
250	1.35×10^5	0.81	0.31	0.30–0.50 ²⁴ ($4.0 \times 10^4 < \text{Re} < 2.0 \times 10^5$)

†Experimental measurements in dish-bottom vessels with a RCI: two beavertail baffles,^{19,20} and a single beavertail baffle,^{21,22}. Experimental measurements in flat- and conical-bottom vessels with a RCI and a single beavertail baffle.²⁴

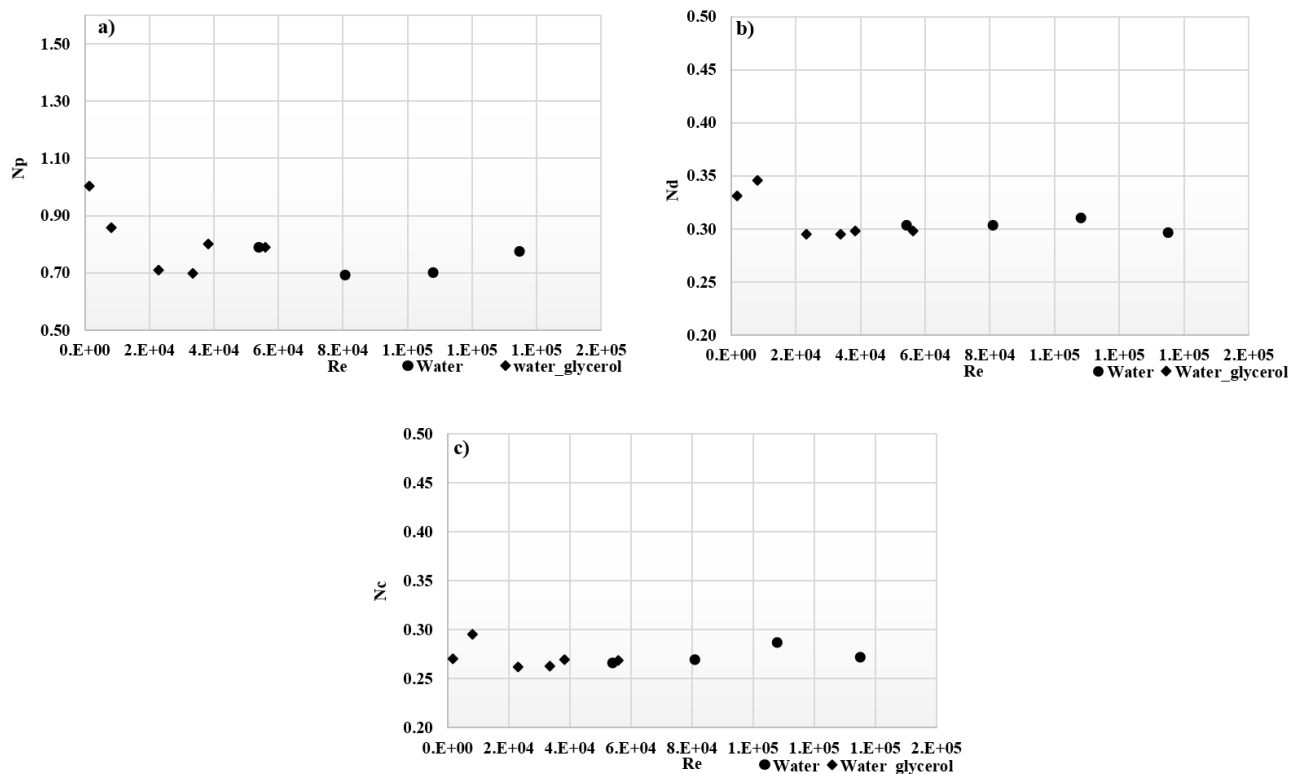


Figure 18. Calculated from CFD predictions (a) Impeller power number, (b) impeller flow number and (c) secondary circulation number as a function of Re (♦ simulations using water-glycerine mixtures and • using pure water).

The simulation results reveal the general trend of variation of the hydrodynamic macro-parameters with Re which are invariant in the fully turbulent condition. As illustrated in Figure 18, N_p decreases with increasing Re for values below 20,000 where the liquid viscosities are higher (mostly for mixtures of water-glycerine), then becomes stable within the turbulent regime ($Re > 20,000$), which is in good agreement with previously reported data for power number. Campolo et al.^{19,20} reported that the measured N_p values for a laboratory-scale flat bottom reactor with a RCI and two beavertail baffles slightly decrease from 0.79 to 0.70 for $10^4 < Re < 10^5$. A single measurement was also given for an industrial-scale reactor with the N_p being equal to 0.76 for similar operating conditions. Dickey et al.²¹ also found that measured N_p decreases from 0.8 to

0.6, for a reactor with a RCI and a single finger baffle. Li et al.²³ reported calculated N_p of around 1.06 with no change in its value for $Re > 10^4$ using CFD without VoF for the same crystalliser used in this study. For both conical and flat reactors with a RCI and different C/T ratios, Rielly et al.²⁴ reported measurements of power number between 0.30 and 0.50, which vary with C/T ratio and type of vessel bottom, but with no evident change as a function of Re .

The present results also fall between those reported for unbaffled and fully baffled reactors which should be expected, as an increase in the number of baffle leads to an increase in power input resulting from the shift from a swirling to a vertical recirculating flow.⁶¹⁻⁶³ Myers et al.⁶⁴ found that changing from four wall-mounted baffles to one resulted in a 60% decrease in the power drawn for a radial flow impeller.

6. CONCLUSIONS

In the initial phase of the work towards developing a CFD-PBM modelling strategy for the digital design and optimisation of crystallisation processes as illustrated in Figure 1, a CFD methodology was established and assessed in order to accurately predict hydrodynamics in a kilo-scale crystalliser with a configuration representative of pharmaceutical crystallisers. The comparison between the predicted mean velocity components against the LDA measurements³¹ reveals that improved predictions are obtained using the RST turbulence model coupled with the VoF method for treating the liquid free-surface and capturing vortex formation compared to those using the SST model and with a flat liquid surface. The turbulence kinetic energy is however significantly underpredicted in the proximity of the impeller which is largely due to the uncertainty in the angle-resolved values extracted from the phase-resolved data. Nevertheless, the RST model underperforms in this region which is rather uncharacteristic of an anisotropic turbulence model. However, the quality of the predictions improves away from the impeller. Improved predictions of turbulence quantities may be obtained through the use of an LES approach but at a prohibitively

high computational cost particularly when a crystallisation process is simulated using a PBM fully integrated with an inhomogeneous multi-phase flow model. This aspect will be explored in our next phase of the work involving CFD-PB modelling of crystallisation processes.

The simulation results using CFD-VoF for different impeller speeds reveal that the vortex formation cannot be prevented by a single baffle and that an accurate representation of the free-surface of the liquid is essential for improved prediction of the flow field in this type of crystalliser. Whilst the vortex depth increases with increasing Re , the predicted trend of the hydrodynamic macro-parameters (such as power number, impeller flow number and secondary circulation flow number) as functions of impeller speed and liquid viscosity show that these parameters are essentially independent of Re in the turbulent regime but fluctuate in the transitional and in the laminar regime. The values of these parameters are necessary for determining the crystalliser operating environment and its scale up as they represent the hydrodynamics and mixing for a given crystalliser geometry, but they are scarce in open literature and are difficult to measure. CFD can be used to create a database that would facilitate crystallisation process development and scale up.

■ AUTHOR INFORMATION

Corresponding author

Tariq Mahmud – *Centre for the Digital Design of Drug Products, School of Chemical and Process Engineering, University of Leeds, Leeds LS2 9JT, U. K.;* orcid.org/0000-0002-6502-907X; Email: t.mahmud@leeds.ac.uk

Authors

Diana Milena Camacho Corzo – *Centre for the Digital Design of Drug Products, School of Chemical and Process Engineering, University of Leeds, Leeds LS2 9JT, U. K.;* orcid.org/0000-0001-5330-4110; Email: dcamachocorzo@gmail.com

Caiyun Ma – *Centre for the Digital Design of Drug Products, School of Chemical and Process Engineering, University of Leeds, Leeds LS2 9JT, U. K.;* orcid.org/0000-0002-4576-7411; Email: C.Y.Ma@leeds.ac.uk

Kevin J. Roberts – *Centre for the Digital Design of Drug Products, School of Chemical and Process Engineering, University of Leeds, Leeds LS2 9JT, U. K.;* orcid.org/0000-0002-1070-7435; Email: k.j.roberts@leeds.ac.uk

Complete contact information is available at:

Notes

The authors declare no competing financial interest.

■ ACKNOWLEDGMENTS

The authors gratefully acknowledge the UK's AMSCI scheme for the financial support of the ADDoPT Project: Towards Digital Design and Operation of Robust Manufacturing Processes for the Pharmaceutical Sector (Grant reference 14060). We also gratefully acknowledge previous UK Engineering and Physical Sciences Research Council (EPSRC) funding which has developed the underpinning capabilities in batch crystallisation scale-up (GR/R/43860/1), crystallisation kinetics (EP/I014446/1) and morphological prediction (EPI028293/1). We thank Professor M. Li, Dr. D. Wilkinson and Professor G. White, CBB-II team members at Heriot-Watt University, Edinburgh, UK, for providing experimental data used in this study.

■ NOMENCLATURE

Symbols

C	Impeller off-bottom clearance	m
C_μ	RST model constant in Eq. (5)	
D	Impeller diameter	m
F_j	Body force term in Eq. (2)	
G_{ij}	Stress production by system rotation term in Eq. (5)	
g_i	Gravitational acceleration	m s^{-2}
H	Stationary liquid height in the vessel	m
k	Turbulence kinetic energy	$\text{m}^2 \text{s}^{-2}$
N	Impeller rotational speed	rpm
N_c	Secondary circulation flow number ($= w_{up}/\rho ND^3$)	
N_d	Impeller flow number ($= w_d/\rho ND^3$)	
N_p	Impeller power number ($= P/\rho N^3 D^5$)	
P	Pressure	Pa
P	Power consumption in the vessel	W
P_{ij}	Stress production term in Eq. (5)	
Re	Reynolds number ($= \rho ND^2/\mu$)	
r	Radius	m
\mathbf{r}	Position vector	
t	Time	s
T	Vessel diameter	m
u_i	Reynolds-average (mean) velocity component	m s^{-1}
u'_i	Fluctuating component of velocity	m s^{-1}
V_{tip}	Impeller tip velocity ($= \pi DN$)	m s^{-1}
w_d	Impeller pumping capacity	kg s^{-1}
w_{up}	Upward axial flow discharged from impeller	kg s^{-1}
x_i	Distance	m
y^*	Dimensionless distance	

Greek Symbols

α	Volume fraction	
δ_{ij}	Kronecker delta	
ε	Turbulence energy dissipation rate	$\text{m}^{-2} \text{s}^{-3}$
ε_{ij}	Viscous dissipation tensor in Eq. (5)	
μ	Viscosity	$\text{kg m}^{-1} \text{s}^{-1}$
ρ	Density	kg m^{-3}
σ_k	RST model constant in Eq. (5)	
τ	Stress tensor	N m^{-2}
ϕ_{ij}	Pressure-strain redistribution term in Eq. (5)	
ω	Angular velocity	radian s^{-1}

Subscripts

a	Air
m	Volume-weighted mixture
q	Gas or liquid phase

w Water

Abbreviations

CFD	Computational fluid dynamics
CSD	Crystal size distribution
DES	Detached-eddy simulation
LDA	Laser Doppler anemometry
LES	Large-eddy simulation
PBM	Population balance model
RANS	Reynolds-averaged Navier-Stokes
RCI	Retreat curve impeller
RST	Reynolds-stress transport
SST	Shear-stress transport
VoF	Volume-of-fluid
UDF	User defined function

■ ASSOCIATED CONTENT

Supporting Information

The Supporting Information is available free of charge at <https://pubs.acs.org/doi/xx.xxxx/acs.oprd.0x00000>.

S1: The derivation of the mathematical model of Nagata¹⁵ to calculate vortex depth for unbaffled vessels and a modification to this model by Smit and During.¹⁶

S2: The derivation of the equation of Deshpande et al.¹⁸ to calculate vortex depth under viscous conditions .

■ REFERENCES

- (1) Schmidt, B.; Patel, J.; Ricard, F. X.; Brechtelsbauer, C. M.; Lewis, N. Application of process modelling tools in the scale-up of pharmaceutical crystallisation processes, *Org. Process Res. Dev.* **2004**, 8, 998-1008.
- (2) Kougolous, E.; Jones, A. G.; Wood-Kaczmar, M. W. Process modelling tools for continuous and batch organic crystallisation processes including application to scale-up. *Org. Process Res. Dev.* **2006**, 10, 739-750.
- (3) Paul, E. L.; Midler, M.; Sun, Y. Mixing in the Fine Chemicals and Pharmaceutical Industries. In *Handbook of Industrial Mixing: Science and Practice*; Paul, E. L., Atiemo-Obeng, V. A., Kresta, S. M., Eds.; John Wiley & Sons, Inc.: Hoboken, **2004**; pp 1027-1069
- (4) McKeown, R. R.; Waterman, J. T.; Dell'Orco, P. C. Crystallization Design and Scale-up. In *Chemical Engineering in the Pharmaceutical Industry: R&D to Manufacturing*; am Ende, D. J., Eds.; John Wiley & Sons, Inc.: New York, **2011**; pp 213-247.
- (5) Costa, C. B. B.; Maciel, M. R. W.; Filho, R. M.; Considerations on the crystallization modeling: Population balance solution. *Comput. Chem. Eng.* **2007**, 31(3), 206-218.
- (6) Kalbasenka, A.; Huesman, A.; Kramer, H. Modeling batch crystallization processes: Assumption verification and improvement of the parameter estimation quality through empirical experiment design. *Chem. Eng. Sci.* **2011**, 66, 4867-4877.
- (7) Shaikh, L. J.; Bari, A. H.; Ranade, V. V.; Pandit, A. B. Generic framework for crystallization processes using the population balance model and its applicability. *Ind. Eng. Chem. Res.* **2015**, 54, 10539-10548
- (8) Rielly, C. D.; Marquis, A. J. A particle's eye view of crystallizer fluid mechanics. *Chem. Eng. Sci.* 2001, 56, 2475-2493.
- (9) Ma, C. Y.; Roberts, K. J. Combining Morphological Population Balances with Face-Specific Growth Kinetics Data to Model and Predict the Crystallization Processes for Ibuprofen. *Ind. Chem. Eng. Res.* **2018**, 57 (48), 16379-16394.
- (10) Ma, C. Y.; Wang, X. Z.; Roberts, K. J. Morphological population balance for modelling crystal growth in individual face directions. *AIChE J.*, **2008**, 54, 209-222.
- (11) Towards Digital Design and Operation of Robust Manufacturing Processes for the Pharmaceutical Sector - Advanced Digital Design of Pharmaceutical Therapeutics (ADDopt), <https://www.addopt.org/>
- (12) Serra, A.; Campolo, M.; Soldati, A. Time-dependent finite-volume simulation of the turbulent flow in a free-surface CSTR. *Chem. Eng. Sci.* **2001**, 56 (8), 2715-2720.
- (13) Haque, J. N.; Mahmud, T.; Roberts, K. J.; Rhodes, D. Modelling turbulent flows with free-surface in unbaffled agitated vessels. *Ind. Eng. Chem. Res.* **2006**, 45, 2881-2891.
- (14) Bentham, E. J.; Heggs, P. J.; Mahmud, T. CFD modelling of conjugate heat transfer in a pilot-scale unbaffled stirred tank reactor with a plain jacket. *Can. J. Chem. Eng.* **2019**, 97, 573-585.
- (15) Nagata, S. *Mixing Principles and Applications*; Halsted Press: New York, 1975.
- (16) Smit, L.; During, J. Vortex geometry in stirred vessels, *Proc. 7th European Conference on Mixing*, Brugge, Belgium, 18-20 September, 1991, 2; pp 633-639.

- (17) Busciglio, A.; Grisafi, F.; Scargiali, F.; Brucato, A. On vortex shape in unbaffled stirred vessels as measured by digital image analysis, *Proc. 14th European Conference on Mixing*, Warszawa, Poland, 10-13 September, 2012; pp 49-54.
- (18) Deshpande, S. S.; Kar, K. K.; Walker, J.; Pressler, J.; Su, W. An experimental and computational investigation of vortex formation in an unbaffled stirred tank. *Chem. Eng. Sci.* **2017**, 168, 495-506.
- (19) Campolo, M.; Paglianti, A.; Soldati, A. Fluid dynamic efficiency and scale-up of a retreated blade impeller CSTR, *Ind. Eng. Chem. Res.* **2002**, 41,164-172.
- (20) Campolo, M.; Soldati, A. Appraisal of fluid dynamic efficiency of retreated-blade and turbofoil impellers in industrial-size CSTRs, *Ind. Eng. Chem. Res.* **2002**, 41, 1370-1377.
- (21) Dickey, D. S.; Bittorf, K. J.; Ramsey, C.J.; Johnson, K. E. Understanding flow patterns in glass-lined reactors. *Chem. Eng. Prog.* **2004**, 100, 21-25.
- (22) Sirasitthichoke, C.; Armenante, P. M. Power dissipation and power number correlations for a retreat-blade impeller under different baffling conditions. *Ind. Eng. Chem. Res.* **2017**, 56, 10123-10133.
- (23) Li, M. Z.; White, G.; Wilkinson, D.; Roberts, K. J. Scale up study of retreat curve impeller stirred tanks using LDA measurements and CFD simulation. *Chem. Eng. J.* **2005**, 108, 81-90.
- (24) Rielly, C. D.; Habib, M. J.; Sherlock, P. Flow and mixing characteristics of a retreat curve impeller in a conical-based vessel. *Chem. Eng. Res. Des.* **2007**, 85(A7), 953-962.
- (25) Cartland Glover, G. M.; Fitzpatrick, J. J.: Modelling vortex formation in an unbaffled stirred tank reactors. *Chem. Eng. J.* **2007**, 127, 11-22.
- (26) Haque, J. N.; Mahmud, T.; Roberts, K. J.; Liang, J. K.; White, G.; Wilkinson, D.; Rhodes, D. Free-surface turbulent flow induced by a Rushton turbine in an unbaffled dish-bottom stirred tank reactor: LDV measurements and CFD simulations. *Can. J. Chem. Eng.* **2011**, 89, 745-753.
- (27) Yang, F. L.; Zhou, S. J.; Zhang, C. X.; Evans, G. M.; Wang, G. C. Study of the turbulent flow in an unbaffled stirred tank by detached eddy simulation, *Chem. Eng. Commun.* **2013**, 200, 1347-1365.
- (28) Yang, F. L.; Zhou, S. J. Free surface turbulent flow in an unbaffled stirred tank: Detached eddy simulation and VOF study. *Chem. Biochem. Eng. Q.* **2015**, 29(3), 395–403.
- (29) Torr , J. P.; Fletcher, D. F.; Lasuye, T.; Xuereb, C. An experimental and computational study of the vortex shape in a partially baffled agitated vessel. *Chem. Eng. Sci.* **2007a**, 62, 1915-1926.
- (30) Torr , J. P.; Fletcher, D. F.; Lasuye, T.; Xuereb, C. Single and multiphase CFD approaches for modelling partially baffled stirred vessels: Comparison of experimental data with numerical predictions. *Chem. Eng. Sci.* **2007b**, 62, 6246-6262.
- (31) Li, M. Z.; White, G.; Wilkinson, D.; Roberts, K. J. LDA measurements and CFD modeling of a stirred vessel with a retreat curve impeller. *Ind. Eng. Chem. Res.* **2004**, 43, 6534-6547.
- (32) Jahoda, M.; Mořt k, M.; Fořt, I.; Hasal, P. CFD simulation of free liquid surface motion in a pilot plant stirred tank, *Can. J. Chem. Eng.* **2011**, 89, 717-724.

- (33) Liang, J. K. Process scale dependence of L-glutamic acid batch crystallised from aqueous solution in relation to reactor internals, reactant mixing and process conditions, Ph.D. Thesis, Heriot-Watt University, UK, 2002.
- (34) Versteeg, H.; Malalasekera, W. *An Introduction to Computational Fluid Dynamics - The Finite Volume Method*, 2nd Ed.; Pearson: Harlow, **2009**.
- (35) Lamarque, N.; Zoppé, O. B.; Lebaigue, O.; Dolias, Y.; Bertrand, M.; Ducros, F. Large-eddy simulation of the turbulent free-surface flow in an unbaffled stirred tank reactor, *Chem. Eng. Sci.* **2010**, 65, 4307-4322.
- (36) Hartmann, H.; Derksen, J. J.; Montavon, C.; Pearson, J.; Hamill, I. S.; van den Akker, H. E. A. Assessment of large eddy and RANS stirred tank simulations by means of LDA. *Chem. Eng. Sci.* **2004**, 59(12), 2419-2432.
- (37) Murthy, B. N.; Joshi, J. B. Assessment of standard $k-\epsilon$, RSM and LES turbulence models in a baffled stirred vessel agitated by various impeller designs. *Chem. Eng. Sci.* **2008**, 63, 5468-5495.
- (38) Gimbut, J.; Rielly, C. D.; Nagy, Z. K.; Derksen, J. J. Detached eddy simulation on the turbulent flow in a stirred tank, *AIChE J.* **2012**, 58(10), 3224-3241.
- (39) Joshi, J. B.; Nere, N. K.; Rane, C. V.; Murthy, B. N.; Mathpati, C. S.; Patwardhan, A. W.; Ranade, V. V. CFD simulation of stirred tanks: Comparison of turbulence models. Part I: Radial flow impellers. *Can. J. Chem. Eng.* **2011**, 89, 23-82.
- (40) Malika, S.; Lévêque, E.; Bouaifib, M.; Gamet, L.; Flottès, E.; Simoëns, S.; El-Hajema, M. Shear improved Smagorinsky model for large eddy simulation of flow in a stirred tank with a Rushton disk turbine. *Chem. Eng. Res. Des.* **2016**, 108, 69-80.
- (41) Zwart, P. J.; Scheuerer, M.; Bogner, M. Numerical modelling of free-surface and cavitating flows. Presented at *ASTAR International Workshop on Advances Numerical Methods for Multidimensional Simulation of Two-Phase Flow*, Germany, 2003.
- (42) Menter, F. R. Two-equation eddy-viscosity turbulence models for engineering applications, *AIAA J.*, **1994**, 32, 1598-1605.
- (43) Wilcox, D. C. Reassessment of the scale-determining equation for advanced turbulence models. *AIAA J.* **1988**, 26, 1299-1310.
- (44) Jones, R. M.; Harvey, A. D.; Acharya, S. Two-equation turbulence modeling for impeller stirred tanks. *J. Fluids Engineering, Transactions of the ASME.* **2001**, 123, 640-648.
- (45) Singh, H.; Fletcher, D. F.; Nijdam, J. J. An assessment of different turbulence models for predicting flow in a baffled tank stirred with a Rushton turbine. *Chem. Eng. Sci.* **2011**, 66, 5976-5988.
- (46) Menter, F. R.; Egorov, Y. The scale-adaptive simulation method for unsteady turbulent flow predictions. Part 1: Theory and model description, *Flow, Turbul. Combust.* **2010**, 85, 113-138.
- (47) Domański, M.; Karcz, J.; Bitenc, M. Scale-adaptive simulation of liquid mixing in an agitated vessel equipped with eccentric HE 3 impeller. *Chemical Papers.* 2014, 68 (7), 899-912, DOI: 10.2478/s11696-014-0546-6
- (48) Daly, B.J.; Harlow, F. H. Transport equations in turbulence, *Phys. Fluids*, **1970**, 13, 2634-2649.

- (49) Launder, B. E.; Reece, G. J.; Rodi, W. Progress in the development of a Reynolds-stress turbulence closure. *J. Fluid Mech.* **1975**, 68, 537-566.
- (50) Speziale, C. G.; Sarkar, S.; Gatski, T. B. Modelling the pressure-strain correlation of turbulence: An invariant dynamical systems approach. *J. Fluid Mech.* **1991**, 277, 245-272.
- (51) Barth, T. J.; Jespersen, D. C. The design and application of upwind schemes on unstructured meshes; AIAA Paper 89-0366; American Institute of Aeronautics and Astronautics: Reston, VA, 1989.
- (52) *Fluent-V17.1 User Manual*; ANSYS: Pittsburgh, USA, 2016.
- (53) Control and scale-up of batch crystallisation processes - Chemicals Behaving Badly II, www.leeds.ac.uk/chemeng/CBB/cbb2.html
- (54) Luo, J. Y.; Gosman, A. D.; Issa, R. I.; Middleton, J. C., Fitzgerald, M. K. Full flow field computation of mixing in baffled stirred vessels, *Trans. Inst. Chem. Eng., Part A Chem. Eng. Res. Des.* **1993**, 71, 342-344.
- (55) Ng, K.; Fentiman, J.; Lee, K. C.; Yianneskis, M. Assessment of sliding mesh CFD predictions and LDA measurements of the flow in a tank stirred by a Rushton impeller, *Chem. Eng. Res. Des.* **1998**, 76A, 737-747.
- (56) Montante, G.; Lee, K. C.; Brucato, A.; Yianneskis, M. Numerical simulations of the dependency of flow pattern on impeller clearance in stirred vessels, *Chem. Eng. Sci.* **2001**, 56 (12), 3751-3770.
- (57) Alcamo, R.; Micale, G.; Grisafi, F.; Brucato, A.; Ciofalo, M. Large-eddy simulation of turbulent flow in an unbaffled stirred tank driven by a Rushton turbine. *Chem. Eng. Sci.* **2005**, 60(8-9), 2303-2316.
- (58) Mahmud, T.; Haque, J. N.; Roberts, K. J.; Rhodes, D.; Wilkinson, D. Measurements and modelling of free-surface turbulent flows induced by a magnetic stirrer in an unbaffled stirred tank reactor, *Chem. Eng. Sci.* **2009**, 64, 4197-4209.
- (59) Jaworski, Z.; Zakrzewska, B. Modelling of the turbulent wall jet generated by a pitched blade turbine impeller – the effect of turbulence model. *Chem. Eng. Res. and Des.* **2002**, 80(A8), 846-854.
- (60) Menter, F. R.; Langtry, R. B.; Likki, S. R.; Suzen, Y. B.; Huang, P. G.; Volker, S. A correlation-based transition model using local variables - Part I: Model formulation. *J Turbomach.* **2006**, 128, 413-422.
- (61) Rushton, J. H.; Costich, E. W.; Everett, H. J. Power characteristics of mixing impellers, part I, *Chem. Eng. Prog.* **1950**, 46(8), 395-404.
- (62) Rushton, J. H.; Costich, E.W.; Everett, H. J. Power characteristics of mixing impellers, part II, *Chem. Eng. Prog.* **1950**, 46(9), 467-476.
- (63) Bates, R. L.; Fondy, P. L.; Corpstein, R. R. An examination of some geometric parameters of impeller power, *I&EC Proc. Des. Dev.* 1963, 2(4), 310-314.
- (64) Myers, K.J.; Reeder, M.F.; Fasano, J. B. Optimize mixing by using the proper baffles, in: *Chem. Eng. Prog. Magazine*, **2002**, pp. 42-47.